Forced Planetary Wave Response in a Thermocline Gyre

ZHENGYU LIU

Department of Atmospheric and Oceanic Sciences, University of Wisconsin—Madison, Madison, Wisconsin

(Manuscript received 30 January 1998, in final form 29 June 1998)

ABSTRACT

The response of a thermocline gyre to anomalies in surface wind stress forcing and surface buoyancy forcing is investigated in light of planetary wave dynamics, both analytically and numerically. The author's theory suggests that anomalous Ekman pumping most efficiently generates the non-Doppler-shift mode, which resembles the first baroclinic mode and has the clearest signal in the sea surface height field and the lower thermocline temperature field. The non-Doppler-shift mode propagates westward rapidly regardless of the mean circulation. In contrast, anomalous surface buoyancy forcing, which can be simulated by an entrainment velocity, produces the strongest response in the advective mode, which resembles the second baroclinic mode and has the largest signature in the upper thermocline temperature field. The advective mode tends to propagate in the direction of the subsurface flow, but its propagation speed may differ substantially from that of the mean flow. The theory is further substantiated by numerical experiments in three ocean models: a 3-layer eddy-resolving quasigeostrophic model, a 2.5-layer primitive equation model, and an oceanic general circulation model. Finally, relevance of the theory to recent observations of decadal variability in the upper ocean and the climate system is also discussed.

1. Introduction

Recent observations have revealed an important aspect of interannual to decadal extratropical thermocline variability, which is that the sea surface height (SSH) anomaly propagates predominantly westward at all latitudes (Jacobs et al. 1994; Chelton and Schlax 1996), while a substantial part of the thermocline temperature variability follows the gyre circulation (Deser et al. 1996; Zhang and Levitus 1997; White and Cayan 1997). This complexity of thermocline variability motivated us to reexamine the dynamics of planetary waves in the presence of a thermocline circulation. Liu (1998) suggested that the different features of variability may be associated with two types of planetary wave modes in the extratropical ocean: the non-Doppler-shift mode (N mode) and the advective mode (A mode). The N mode resembles the first baroclinic mode and propagates westward regardless of the mean flow. The A mode resembles the second baroclinic mode and tends to follow the mean flow. Furthermore, because of the distinct vertical structure of the two modes, it is speculated that the N mode is mostly responsible for the observed SSH variability, while the A mode is predominantly responsible for observed temperature variability in the upper thermocline.

In this study, we extended the results of Liu (1998) by first generalizing the basic state of the zonal flow to a more realistic thermocline gyre circulation. More importantly, we investigated the response of the thermocline to anomalies of surface dynamic forcing and buoyancy forcing in light of planetary wave dynamics. We found that anomalous Ekman pumping is the most efficient mechanism for generating the N mode with the clearest signal in the SSH field, while anomalous surface buoyancy forcing may be important for producing the A mode with a strong temperature signal in the upper thermocline.

The paper is arranged as follows: Section 2 introduces the model. Section 3 investigates the propagation of planetary waves in a thermocline gyre circulation. Section 4 further studies the generation mechanism of planetary waves by both the surface wind stress forcing and surface buoyancy forcing. Supporting experiments with three numerical models are presented in section 5. A further discussion on the dynamics of the A mode is presented in section 6. In section 7, we provide a summary and some further discussion of the relevance of our results to observations.

2. The model

To highlight the physical mechanisms involved, we used a 2.5-layer QG model as in Liu (1998). The densities for layer 1 (upper thermocline), layer 2 (deeper thermocline), and layer 3 (abyss) are assumed as $\rho_1 = \rho - 2\Delta\rho$, $\rho_2 = \rho - \Delta\rho$, and $\rho_3 = \rho$. The thicknesses

Corresponding author address: Z. Liu, Department of Atmospheric and Oceanic Sciences, University of Wisconsin—Madison, 1225 W. Dayton St., Madison, WI 53706.
E-mail: znl@ocean.meteor.wisc.edu

for layers 1 and 2 are D_1 and D_2, respectively. Under a surface Ekman pumping w_e and an entrainment velocity w_d between layers 1 and 2, the nondimensional QGPV 2.5-layer model can be derived as (§6.16 of Pedlosky 1987; Liu 1998)

$$[\partial_t + J(\psi_1,)]q_1 = (\mathbf{w}_e - \mathbf{w}_d)/d_1, \qquad (2.1a)$$

$$[\partial_t + J(\psi_2,)]q_2 = \mathbf{w}_d/d_2. \qquad (2.1b)$$

Here $q_1 = y + (\psi_2 - \psi_1)/d_1$ and $q_2 = y + (\psi_1 - 2\psi_2)/d_2$ are the potential vorticities of layers 1 and 2, respectively. Note that the relative vorticity is neglected because we are interested only in planetary waves. The nondimensional layer thicknesses are $d_n = D_n/(D_1 + D_2)$ $(n = 1, 2)$. Other nondimensionl variables are represented by their dimensional counterparts (in "*") as

$$(x, y) = (x^*, y^*)/L, \qquad t = t^*/T, \qquad \psi_n = \psi_n^*/V_s L,$$

$$\mathbf{w}_e = \mathbf{w}_e/W, \qquad \mathbf{w}_d = \mathbf{w}_d^*/W.$$

Here L is the gyre scale, $V_s = \beta L_D^2$ is a typical speed, $T = L/V_s$ is the timescale of gyre advection, and W is the magnitude of Ekman pumping that satisfies the Sverdrup balance as $\beta V_s(D_1 + D_2) = f_0 W$. In addition, $L_D = [g'(D_1 + D_2)]^{1/2}/f_0$ and $g' = g\Delta\rho/\rho$ are the baroclinic deformation radius and the reduced gravity, respectively. Typical parameters in the midlatitudes are $\Delta\rho/\rho = 0.002$, $f_0 = 10^{-4}$ s^{-1}, $\beta = 1.2 \times 10^{-11}$ m^{-1} s^{-1}, $D_1 + D_2 = 1000$ m, which give $L_D = 45$ km, $V_s = 0.025$ m s^{-1}, and $W = 3 \times 10^{-6}$ m s^{-1}. Finally, the equivalent dynamic elevations on the surface and the two interfaces are $h_1 = \psi_1$, $h_2 = \psi_2 - \psi_1$, and $h_3 = -\psi_2$.

Surface dynamic forcing is Ekman pumping in a QG model. Surface buoyancy forcing is parameterized as an entrainment velocity $\mathbf{w}_d$ at the interface of layers 1 and 2. This parameterization can be understood as follows. Convection due to surface cooling generates a low PV anomaly that will be ventilated into the lower thermocline (layer 2 in our model). In a planetary geostrophic model that allows explicit outcropping, the cooling forcing can be represented by the motion of the outcrop line (Liu and Pedlosky 1994; Marshall and Marshall 1995); this motion, however, is difficult to represent properly in our QG model. Nevertheless, we speculate that the low PV anomaly along the outcrop line can be crudely simulated by a detrainment $\mathbf{w}_d < 0$ from layer 1 to layer 2, beneath the base of the mixed layer.[1] This speculation is implied from the solution of Liu and Pedlosky (1994). Our speculation has been confirmed by two recent works that use idealized ventilated thermocline models (Schneider et al. 1998; Huang and Pedlosky 1998) and will also be confirmed in a full ocean general circulation model later in section 5.

For small amplitude disturbances ϕ_n, we have $\psi_n = \Phi_n(x, y) + \phi_n(x, y, t)$ $(n = 1, 2)$, where Φ_n is the mean flow streamfunction and $\phi_n \ll \Phi_n$. Similarly, the forcing is separated into mean and perturbation components: $w_e = W_e + w_e$ and $w_d = W_d + w_d$. The linearized perturbation PV equations can therefore be obtained from (2.1a), (2.1b) as

$$(\partial_t + U_1\partial_x + V_1\partial_y)q_1 + J(\phi_1, Q_1) = (w_e - w_d)/d_1, \qquad (2.2a)$$

$$(\partial_t + U_2\partial_x + V_2\partial_y)q_2 + J(\phi_2, Q_2) = w_d/d_2, \qquad (2.2b)$$

where the mean currents are $(U_n, V_n) = (-\partial_y\Phi_n, \partial_x\Phi_n)$ $(n = 1, 2)$; the mean PVs are $Q_1 = y + (\Phi_2 - \Phi_1)/d_1$ and $Q_2 = y + (\Phi_1 - 2\Phi_2)/d_2$; and the perturbation PVs are $q_1 = (\phi_2 - \phi_1)/d_1$ and $q_2 = (\phi_1 - 2\phi_2)/d_2$.

Planetary waves will be studied using the WKB method (Lighthill 1979). For waves with spatial scales much smaller than that of the mean flow, the mean flow and PV gradient can be regarded as locally homogeneous in (2.2). This assumption can be applied to perturbations measuring hundreds of kilometers as shown by altimeter observations (Jacobs et al. 1994; Chelton and Schlax 1996) because the gyre width is on the order of thousands of kilometers. For even larger-scale waves, the WKB approximation may not be very accurate and should be explored in detail in a future study. Nevertheless, the WKB method used here should qualitatively shed light on some basic features of planetary waves, as has been seen in previous studies of Rossby waves (e.g. Hoskins and Karoly 1981). Furthermore, the qualitative conclusions from the WKB solution will be substantiated in section 5 with experiments using three numerical models.

Given the perturbation as

$$\phi_n = \phi_n' e^{i\theta(x,y,t)} \qquad (n = 1, 2),$$

$$w_e = w_e' e^{i\theta(x,y,t)}, \qquad w_d = w_d' e^{i\theta(x,y,t)},$$

where the amplitudes (in prime) are locally constant (the prime will be dropped hereafter without confusion), the WKB solution at the first order yields

$$(U_1 k + V_1 l - \sigma)[(\phi_2 - \phi_1)/d_1] + \phi_1 R_1 = -i(w_e - w_d)/d_1, \qquad (2.3a)$$

$$(U_2 k + V_2 l - \sigma)[(\phi_1 - 2\phi_2)/d_2] + \phi_2 R_2 = -iw_d/d_2, \qquad (2.3b)$$

where $k = \partial_x\theta$, $l = \partial_y\theta$, $\sigma = -\partial_t\theta$ are local wavenumbers and frequency. In addition,

$$R_1 = k\partial_y Q_1 - l\partial_s Q_1 = k + [(U_1 - U_2)k + (V_1 - V_2)l]/d_1,$$

$$R_2 = k\partial_y Q_2 - l\partial_x Q_2 = k + [(2U_2 - U_1)k + (2V_2 - V_1)l]/d_2$$

[1] This w_d is usually thought as cooling ($\mathbf{w}_d < 0$) or warming ($\mathbf{w}_d > 0$) at the interface. It should also be noted that $\mathbf{w}_d$ is the diabatic mass transfer between layer 1 and layer 2, both below the mixed layer. This differs from the subduction velocity that transfers mass adiabatically between the mixed layer and the layer below (Nurser and Marshall 1991).

represents the advection on the mean PV field by the perturbation flows. In the absence of forcing, $w_e = w_d = 0$, (2.3) gives the dispersion relationship for planetary waves

$$A(\sigma, k, l) = 0, \tag{2.4}$$

where

$$A(\sigma, k, l) \equiv \sigma^2 + \sigma[k(1 + d_1) - kU_2 - lV_2] + k(kd_1d_2 - kU_B - lV_B). \tag{2.5}$$

Here $(U_B, V_B) = (d_1U_1 + d_2U_2, d_1V_1 + d_2V_2)$ is the vertically averaged flow within the thermocline. The structure of a planetary wave mode can be shown to satisfy

$$a \equiv \phi_2/\phi_1 = -kd_1/(\sigma + kd_2). \tag{2.6}$$

3. Planetary wave propagation in a thermocline gyre

We first study the propagation of planetary waves in a gyre circulation. This is important to understand the remote response, or teleconnection, in the upper ocean, as has been studied extensively in the atmosphere (Hoskins and Karoly 1981; Wallace and Gultz 1981). Consider a patch of anomalous forcing, which locally has the form

$$w_e = w'_e e^{i(mx+ny-\omega t)}, \qquad w_d = w'_d e^{i(mx+ny-\omega t)}, \tag{3.1}$$

where without loss of generality, $\omega > 0$ is assumed. (The prime will be dropped later without confusion.) This forcing generates planetary waves to radiate away from the forced region. In our 2.5-layer model, the frequency of the two modes should be the same as that of the forcing:

$$\sigma = \omega. \tag{3.2a}$$

The wavenumber along the edge of the local forcing should also be the same as that of the forcing. Here, for simplicity, we will only focus on the waves that radiate from a meridional section $x = x^*$, such as the eastern boundary or the eastern/western edges of the forcing patch (which is assumed to have a straight meridional section as its eastern/western edges). Therefore, we have the condition of the matching of initial meridional wavenumber as

$$l = n. \tag{3.2b}$$

The initial zonal wavenumber can be solved from the dispersion relationship (2.4) as

$$k_N = \{-[(1 + d_1 - U_2)\omega - nV_B] + \Delta\} \div (d_1d_2 - U_B) \tag{3.3a}$$

$$k_A = \{-[(1 + d_1 - U_2)\omega - nV_B] - \Delta\} \div (d_1d_2 - U_B), \tag{3.3b}$$

where $\Delta = \{[(1 + d_1 - U_2)\omega - nV_B]^2 - 4(d_1d_2 - U_B)\omega(\omega - nV_2)\}^{1/2}$ using (3.2a,b). The subscripts N and A denote the N mode and the A mode, respectively. The structure of each mode can be derived from (2.6) as

$$a_* \equiv \phi_{2*}/\phi_{1*} = -k_*d_1/(\sigma + k_*d_2), \tag{3.4}$$

where $* = N$ or A. In this paper, we will limit ourselves to the case of real k in (3.3). In other words, we do not consider the region of very strong westward flow, such as the southwestern part of the subtropical gyre (in the Northern Hemisphere) where planetary waves are destabilized [see Liu (1998) for more details on planetary wave instability].

The propagation of the waves can be studied using the ray tracing theory (Lighthill 1979). Since the mean flow field does not change with time, the frequency of the radiating wave should remain unchanged as in Eq. (3.2a). However, since the mean flow varies in the x as well as the y directions, both k and l will vary along a ray path. By virtue of the dispersion relationship (2.4), the ray tracing equations can be written as

$$\dot{x} = C_{gx} \equiv \partial_k\sigma = [U_2 - (1 + d_1)]\omega + 2k(U_B - d_1d_2) + lV_B]/D \tag{3.5a}$$

$$\dot{y} = C_{gy} \equiv \partial_l\sigma = [V_2\omega + kV_B]/D \tag{3.5b}$$

$$\dot{k} = -\partial_x\sigma = -[(k\partial_xU_2 + l\partial_xV_2)\omega + k(k\partial_xU_B + l\partial_xV_B)]/D \tag{3.5c}$$

$$l = [\omega^2 + (1 + d_1 - U_2)k\omega + (d_1d_2 - U_B)k^2] \div (V_2\omega + V_Bk), \tag{3.5d}$$

where $\dot{} = d/dt$ and $D = 2\omega - [kU_2 + lV_2 - (1 + d_1)k]$. Note that (3.5d) is derived by simply solving the dispersion relationship (2.4). The group velocity can be verified to satisfy $C_{gx}/(\omega/k) + C_{gy}/(\omega/l) = 1$. For a wave ray that starts from (x_0, y_0) at $t = 0$, the complete initial conditions for the wave ray are

$$x = x_0, \qquad y = y_0, \qquad k = k^*, \qquad l = n, \tag{3.6}$$

where $* = N$ for the N-mode wave ray and $* = A$ for the A-mode wave ray; we have also used (3.2b) and (3.3a,b).

We give one example to demonstrate the major features of wave propagation. The basic-state ventilated thermocline is derived as in Hendershoot (1989) under a zonal outcrop line $y_0 = \text{const}$ and mean Ekman pumping $W_e(y) = W_{e0}\sin(y\pi)$. The thermocline solution is

$$\Phi_1 = -d_2y, \qquad \Phi_2 = [d_1d_2y + xW_e(y)]/d_2 \quad \text{for } x < x_S(y) \text{ in the ventilated zone;} \tag{3.7a}$$

$$\Phi_1 = -xW_e(y)]/d_1, \qquad \Phi_2 = 0, \quad \text{for } x_S(y) < x < 0 \text{ in the shadow zone.} \tag{3.7b}$$

Here $x_E = 0$ is the eastern boundary and $x_s(y) = d_1d_2(y_0 - y)/W_e(y)$ is the shadow zone boundary. The parameters are chosen as $W_{e0} = -0.2$, $y_0 = 0.9$, and $d_1 =$

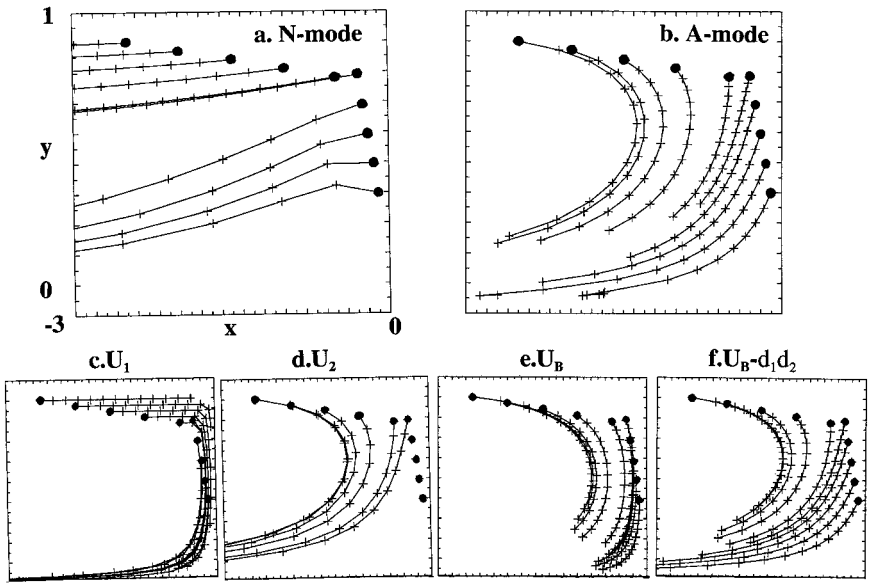

FIG. 1. Wave rays in a ventilated thermocline. Six rays start in the ventilated zone, while the other four originate from the shadow zone, as marked by the heavy dots. The forcing frequency is $\omega = 1$ (decadal) and the initial meridional wavenumber is $n = 3$. (a) N-mode wave rays and (b) A-mode wave rays. The streamlines starting from the same locations are also plotted for (c) the mean flow of layer 1, (d) layer 2, (e) the barotropic flow, and (f) the wave characteristics ($U_B - d_1 d_2$, V_B). The time between each pair of marks is 0.3.

0.4. [See Hendershoot (1989) for more details.] A decadal frequency forcing ($\omega = 1$) is used. The distinctive ray pathways of the two modes can be seen clearly in Figs. 1a and 1b for the wave rays of the N mode and A mode, respectively. Ten wave rays are plotted in each panel. Six rays start near the outcrop line (solid circles) in the ventilated zone where flows originate from the subduction of the mixed layer waters. Four rays originate near the eastern boundary in the shadow zone where there is no flow in the subsurface (Luyten et al. 1983). For comparison, mean flow trajectories are also plotted in Figs. 1c–e following the streamlines of layers 1, 2, and barotropic flow, respectively. In addition, the trajectories that follow the 2-layer wave characteristics ($U_B - d_1 d_2$, V_B) (Rhines 1986; Dewar 1989; Liu 1996) are also plotted in Fig. 1f. These wave characteristics are parallel to the mean subduction flow $\mathbf{U}_2$ in the ventilated zone in a 2.5-layer model (Luyten and Stommel 1986).

Figure 1 shows that, despite the eastward flow in the northern part of the subtropical gyre in all the flow fields (Figs. 1c–e), all the N-mode wave rays propagate westward (Fig. 1a). This is caused by the non-Doppler-shift effect in this mode.[2] In contrast, all the A-mode wave rays tend to follow the mean circulation due to its advective nature (Fig 1b). A comparison of the A-mode wave rays with other trajectories clearly shows that the path of the A-mode wave rays closely resembles that of the wave characteristics (Fig. 1f) or the subsurface subduction flow in the ventilated zone (Fig. 1d).

The relationship between the wave rays and the mean-flow trajectories is seen more clearly in Figs. 2 and 3. Figure 2a shows two wave rays (the two marked curves), one for the N mode and the other for the A mode, which originate in the ventilated zone near the outcrop line. For comparison, we also plotted the trajectories that follow the mean flow of layer 1 (curve with *) and layer 2 (curve with ○). In addition, the wave characteristics ($U_B - d_1 d_2$, V_B) (curve with ×) are also plotted. It is clear in Fig. 2a that the N-mode wave ray does not follow the circulation at all. The A-mode wave ray, on the other hand, follows closely the characteristics ($U_B - d_1 d_2$, V_B) or subsurface ventilation flow $\mathbf{U}_2$, but deviate significantly from the surface flow $\mathbf{U}_1$. This independence of the A-mode wave speed from the surface flow was noted in Liu (1998). Furthermore, the wavenumbers k (solid), l (curve with ○), and the wave structure ($a = \phi_2/\phi_1$) are also shown in Figs. 2b and 2c for the N mode and A mode, respectively. The vertical structure of the wave remains as $a_N > 0$ for the N mode and $a_A < 0$ for the A mode. Thus, the perturbation flows of the two layers are in the same direction for the N mode, but are in the opposite directions for the A mode. Therefore, the N mode resembles the first mode, while the A mode resembles the second mode, as discussed in Liu (1998). Figures 2b and 2c also show that the

[2] Here, we refer to the non-Doppler-shift effect only in a crude sense. Indeed, it has been shown that the wave speed can be enhanced significantly by the mean flow (Killworth et al. 1997; Dewar 1998; Singh 1997; Liu 1998).

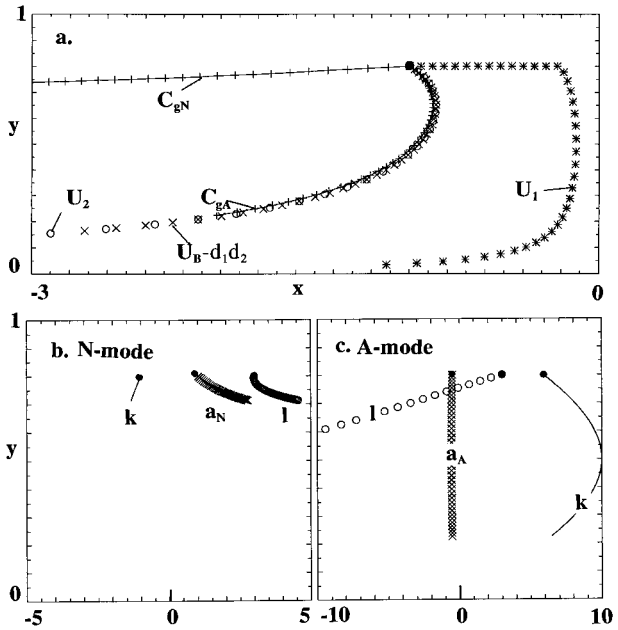

FIG. 2. Wave rays, wavenumbers, and the vertical structure of the waves starting from one location in the ventilated zone. The mean thermocline is the same as in Fig. 1. (a) Plots of the two wave rays ("+" connected curve) as well as the trajectories following $\mathbf{U}_1$ (*), $\mathbf{U}_2$ (○), and ($U_B - d_1d_2$, V_B) (×). (b) The variation of wavenumber k (solid), l (○), and wave structure $a_N = h_{2N}/h_{1N}$ with y, following the N mode. (c) The same as (b) but for the A mode. The time interval between each pair of marks is 0.2. In (b) and (c) the vertical axis is y, and the horizontal axis is nondimensional wavenumber and the ratio of velocities $a = \phi_{2*}/\phi_{1*}$.

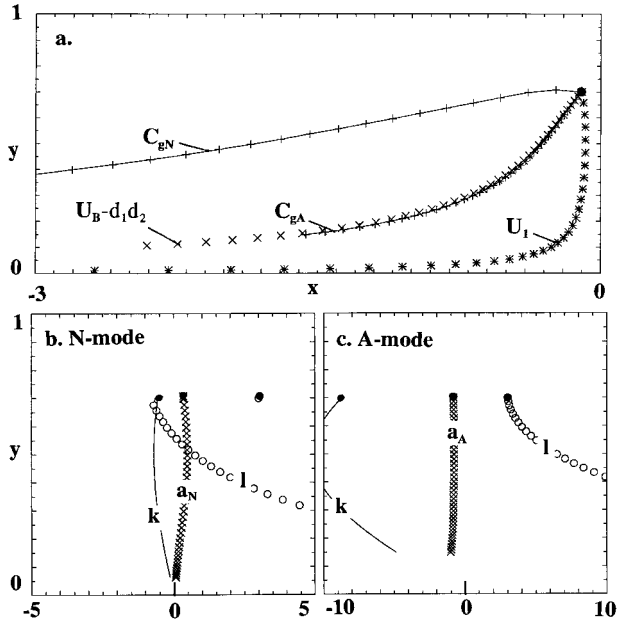

FIG. 3. As in Fig. 2 but initially starting from a position within the shadow zone.

meridional wavenumber l changes significantly, while the zonal wavenumber k does not. This is to be expected because the variation of the mean flow is much stronger in the y direction than in the x direction. This may imply that our WKB approximation is less accurate in the y direction than in the x direction.

To illustrate the trajectory from a shadow zone, we plot trajectories in Fig. 3 the same as in Fig. 2 but for trajectories originating in the shadow zone. The most noticeable difference from Fig. 2 is that, despite the absence of the layer-2 mean flow in the shadow zone, the A mode still propagates roughly along the wave characteristics. Therefore, the characteristics ($U_B - d_1d_2$, V_B) are a more general indicator for the wave rays of the A mode than the subsurface flow. This also indicates a difference between the A mode and a passive tracer. A passive tracer, if started in the shadow zone, will stay in the initial position because of the absence of subsurface flow; this relationship will be further discussed later in section 6.

The conclusions above are not very sensitive to model parameters. Sensitivity experiments were carried out on the forcing frequency ω, the initial meridional wavenumber n, and the mean stratification d_1. For a typical thermocline stratification ($d_1 \sim d_2$), our conclusions above regarding the wave ray, especially in the A mode, remain robust. This is also reinforced in an analytical study outlined in appendix C. Figure 4 shows a sensitivity test of the frequency for a wave ray originating in the ventilated zone (Figs. 4a,b) and the shadow zone (Figs. 4c,d). In both zones, the direction of the N-mode wave ray changes only modestly with the frequency (Figs. 4a,c), and the direction of the A-mode wave ray shows virtually no change. In a typical thermocline gyre, the slope of the A-mode ray can be shown to follow that of ($U_B - d_1d_2$, V_B) within 10%–20% (see appendix C).

Finally, the wave propagation features discussed above can be proven analytically in the limit of low-frequency forcing $\omega \to 0$. In this limit, we have from (2.4) or (3.3a,b) the wavenumber solutions for the two modes as

$$k_N = -(V_2/V_B)\omega + O(\omega^2) \tag{3.8a}$$

$$k_A = -lV_B/(U_B - d_1d_2) + O(\omega). \tag{3.8b}$$

The group velocities and wave structures for the two modes can therefore be derived from (3.5a,b) and (3.4). Using (3.8a), the N mode has at the leading order the group velocity

$$(C_{gxN}, C_{gyN}) = (-1, 0)F_N, \quad \text{where} \quad F_N = V_B/V_2 \tag{3.9a}$$

and the wave structure

$$\phi_{2N}/\phi_{1N} = V_2/V_1. \tag{3.9b}$$

With (3.8b), the A mode has the leading order representation of the group velocity

$$(C_{gxA}, C_{gyA}) = (U_B - d_1d_2, V_B)F_A, \tag{3.10a}$$

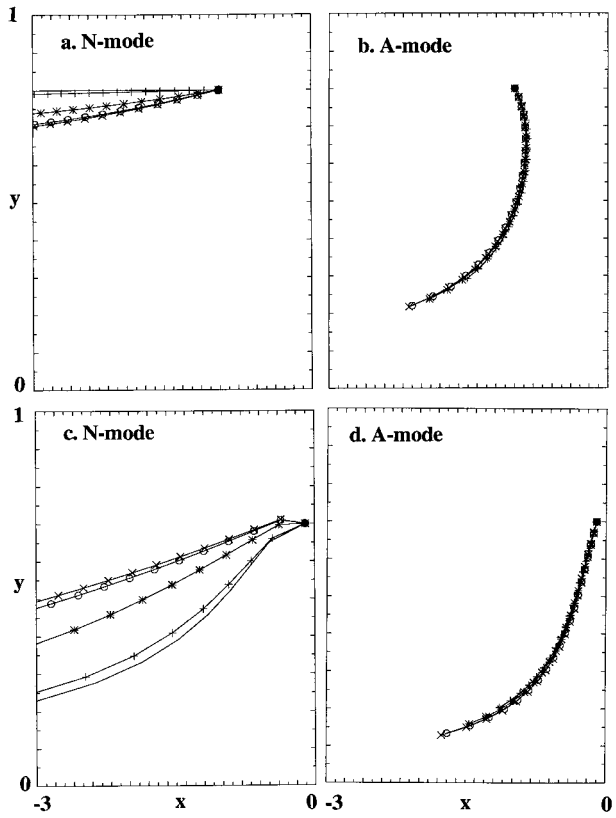

FIG. 4. Sensitivity of wave rays to five frequencies (solid, "+," "*," "○," and "×" for $\omega = 0.01$, 0.1, 1, 5, and 10, respectively). The mean thermocline is the same as in Fig. 1. (a) N mode starting in the ventilated zone, (b) A mode starting in the ventilated zone, (c) N mode starting in the shadow zone, and (d) A mode starting in the shadow zone. The time interval between each pair of marks is 0.2.

where $F_A = V_B/[V_2(U_B - d_1d_2) + V_B(1 + d_1 - U_2)]$ and wave structure

$$\phi_{2A}/\phi_{1A} = -d_1/d_2. \tag{3.10b}$$

The most striking feature is that, regardless of the mean circulation structure, the N-mode wave ray is purely zonal as shown in (3.9a), while the A-mode wave ray is exactly parallel to the wave characteristic ($U_B - d_1d_2$, V_B) as in (3.10a). Furthermore, the N mode has an equivalent barotropic wave structure as shown in (3.9b), while the A mode has a pure baroclinic wave structure (with a zero barotropic transport) as indicated by (3.10b). The wave ray directions and wave structures are consistent with the nature of the two modes that are discussed regarding Figs. 1–4. More specifically, since in the subtropical gyre V_B, $V_2 < 0$ (unless in the shadow zone where $V_2 = 0$), we have $F_N > 0$ in (3.9a). Thus, the N mode propagates purely westward, as expected from the non-Doppler-shift nature of the N mode. However, the propagation speed could vary with the mean flow. In the ventilated zone (3.7a), we have the speed factor $F_N = d_2$. For the A mode, in both the ventilated zone (3.7a) and the shadow zone (3.7b), one can show that the speed factor is $F_A = 1/(1 + d_1) < 1$. Thus, the wave ray is somewhat slower than the wave characteristics as seen in Figs. 1–3. We will return to the wave speed later in section 6.

In short, the N mode propagates westward regardless of the mean flow, while the A mode follows closely ($U_B - d_1d_2$, V_B), which in the ventilated zone is parallel to the mean ventilation flow in layer 2. The conclusions above are not limited to a ventilated thermocline; see a similar discussion regarding the Rhines–Young pool in appendix B. Furthermore, similar conclusions can be obtained in a 3.5-layer model (appendix D).

4. Local response under wind and buoyancy forcing

We further investigate the forcing mechanism of the planetary wave modes. We will study the structure of the locally forced response to anomalies of Ekman pumping and surface buoyancy forcing by projecting the local response onto the two dynamic modes. Using forcing of the form of (3.1), the forced local response is derived from (2.3) as

$$\phi_{1F} = i[(mU_1 + nV_1 - d_2m - 2\omega)w_e + (\omega + d_2m)w_d] \div A(\omega, m, n), \tag{4.1a}$$

$$\phi_{2F} = i[(mU_2 + nV_2 - \omega)w_e - d_1mw_d]/A(\omega, m, n), \tag{4.1b}$$

where A is given in (2.5). This local response is projected onto the two dynamic modes (3.3a,b) as

$$\phi_{1F} = \phi_{1N} + \phi_{1A}, \qquad \phi_{2F} = \phi_{2N} + \phi_{2A}. \tag{4.2}$$

With the aid of (3.4), the modal projection is uniquely determined from (4.2) as

$$\phi_{1N} = (\phi_{2F} - a_A\phi_{1F})/(a_N - a_A),$$
$$\phi_{1A} = (\phi_{2F} - a_N\phi_{1F})/(a_A - a_N), \tag{4.3}$$

and $\phi_{2N} = a_N\phi_{1N}$, $\phi_{2A} = a_A\phi_{1A}$.

Some general results of this forced response can be speculated according to the vertical structures of the wave modes and the surface forcing. On the wave side, within the thermocline, the N mode tends to have a barotropic flow structure, while the A mode has a baroclinic structure, as seen in Liu (1998) and Figs. 2b,c and 3b,c. Furthermore, the strongest amplitude occurs in SSH for the N mode and in thermocline temperature for the A mode. On the forcing side, Ekman pumping has a strong projection component that is barotropic within the thermocline, while entrainment shows a purely baroclinic forcing within the thermocline. Therefore, the vertical structure seems to match between the N mode and Ekman pumping, and between the A mode and entrainment forcing. This suggests a distinct modal response: Ekman pumping most efficiently generates the N mode, while entrainment forcing most effectively forces the A mode.

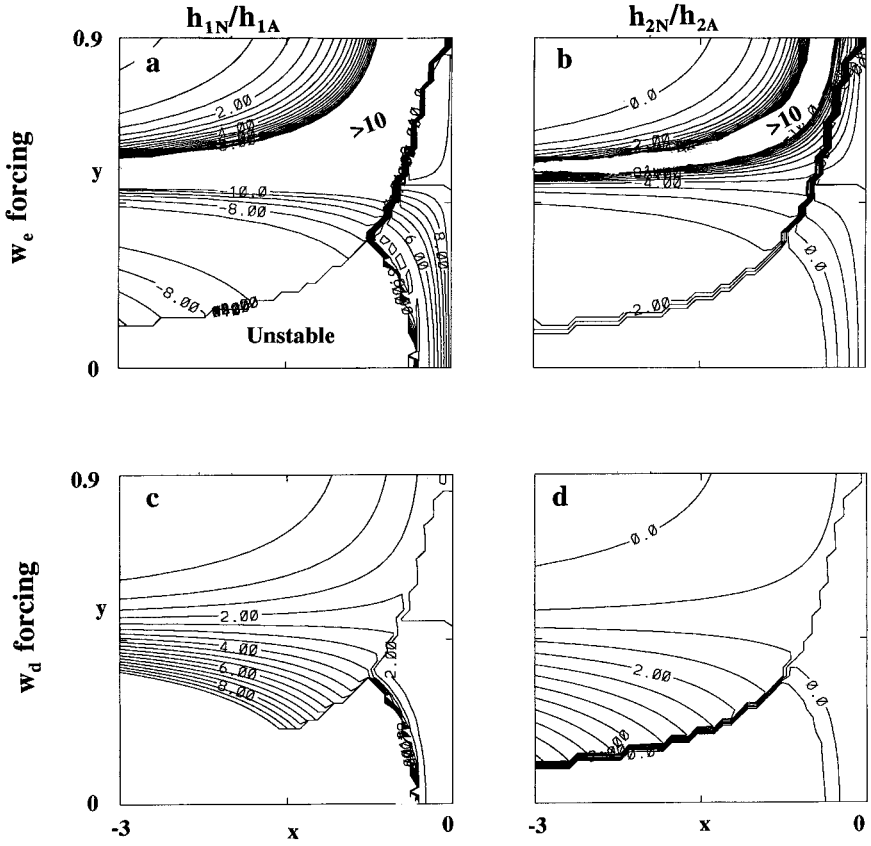

FIG. 5. The ratio of modal projections of the N mode and the A mode under spatially uniform forcing ($m = n = 0$). (a) h_{1N}/h_{1A} for w_e forcing (b) h_{2N}/h_{2A} for w_e forcing, (c) h_{1N}/h_{1A} for w_d forcing, and (d) h_{2N}/h_{2A} for w_d forcing. The contour interval is 0.5. Two regions are not plotted: the region with values greater than 10 and the southwestern part where instability occurs. Ekman pumping forcing mainly generates the N mode as shown in SSH (a), while entrainment forcing mainly forces the A mode in the thermocline temperature (d). Contour interval is 0.5. The mean thermocline is the same as in Fig. 1.

This modal response can also be seen in a more generalized thermocline circulation. Indeed, in a region of weak subsurface flow such as a shadow zone, we have (see appendix A)

$$|h_{1N}/h_{1A}| > 1, \qquad w_e \text{ forcing } (w_d = 0) \qquad (4.4a)$$

$$|h_{2N}/h_{2A}| < 1, \qquad w_d \text{ forcing } (w_e = 0). \qquad (4.4b)$$

As an example, Fig. 5 plots the ratio of the amplitude of the N mode over the A mode under spatially uniform Ekman pumping and entrainment forcing in the basin. Under Ekman pumping forcing (Figs. 5a,b), the SSH is overwhelmed by the N mode, as in (4.4a), over almost the entire basin. In the shadow zone, the ratio $|h_{1N}/h_{1A}|$ ($=|\phi_{1N}/\phi_{1A}|$ in the QG model here) exceeds 5 (the unstable region in the southwest is not discussed here). In the ventilated zone, a very large $|h_{1N}/h_{1A}|$ occurs in a belt that extends from the northwest into the midwest of the gyre. This high $|h_{1N}/h_{1A}|$ belt is caused by a virtually vanishing h_{1A} (not shown). The ratio of the two h_2 does not show such a dramatic difference except in a belt that extends from the northeast to the mid west.

The response is completely different under entrainment forcing (Figs. 5c,d). The ratio of the h_2 response is dominated by the A mode, as in (4.4b) near the outcrop line and in the shadow zone. The SSH, however, does not show such a strong difference in modal response.

These modal responses are not very sensitive to model forcing parameters. Figures 6 and 7 show some sensitivity tests in which the forcing has a spatial structure of $m = 3$, $n = 3$. In addition, three forcing frequencies are used, $\omega = 0.1$, 1, and 10, corresponding to centennial, decadal, and annual times respectively. Under Ekman pumping forcing, the modal response of SSH is shown along the eastern boundary and the outcrop line in Figs. 6a and 6c, respectively. As in the case of Fig. 5, the SSH response is overwhelmed by the N mode ($|h_{1N}/h_{1A}| \gg 1$) for all the frequencies (except in the very western part of the outcrop line). Relatively speaking, the upper thermocline temperature variation $|h_{2N}/h_{2A}|$ is less dominated by the N mode (Figs. 6c,d).

By comparison, under entrainment forcing (Figs.

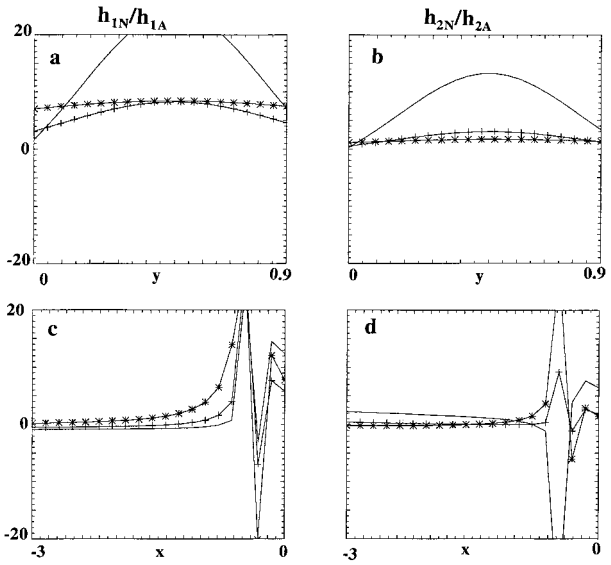

FIG. 6. Sensitivity of the model response to Ekman pumping ($m = 3$, $n = 3$) with different frequencies (solid for $\omega = 0.1$, "+" for $\omega = 1$, and "*" for $\omega = 10$). The mean thermocline is the same as in Fig. 1. (a) h_{1N}/h_{1A} and (b) h_{2N}/h_{2A} are along the eastern boundary $x = 0$, while (c) h_{1N}/h_{1A} and (d) h_{2N}/h_{2A} are near the outcrop line $y = 0.81$.

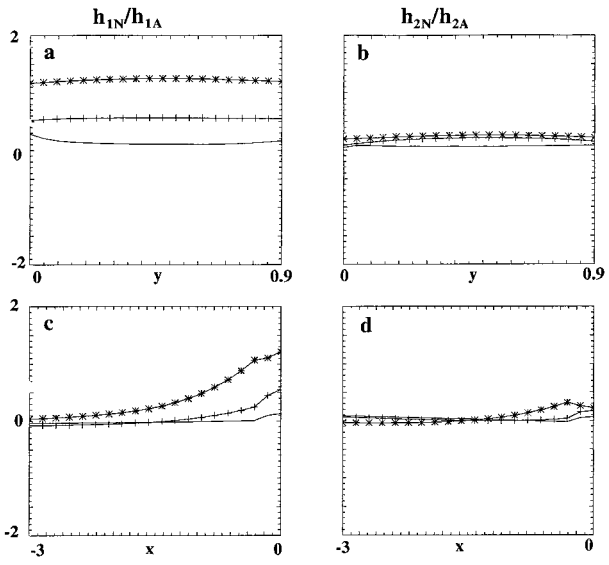

FIG. 7. The same as Fig. 6 but under entrainment forcing.

7b,d), the A mode has the strongest response in the upper thermocline temperature ($|h_{2N}/h_{2A}| \ll 1$) along the eastern boundary and along the outcrop line (note the vertical scale is one order smaller in Fig. 7 than in Fig. 6). Nevertheless, the A mode becomes almost comparable to the N mode in SSH (Figs. 7a,c). These features agree with our earlier discussions (see Figs. 5c,d).

Based on the discussions in the last two sections, we offer a speculative synthesis of thermocline variability from the viewpoint of planetary waves. Ekman pumping is efficient in generating the N mode, which propagates westward rapidly along all latitudes and has the clearest signal in the SSH field. Surface buoyancy forcing (or entrainment forcing here), however, tends to generate a strong A mode that tends to follow the subsurface circulation, or more generally, the characteristics ($U_B - d_1 d_2$, V_B), and has the strongest signature in the thermocline temperature.

5. Numerical experiments

To support our WKB analysis, we present numerical experiments in three models: a 3-layer eddy-resolving QG model in an idealized sector basin, a 2.5-layer primitive equation model for the North Pacific, and a 13-layer Miami Isopycnal Model (MICOM, Bleck et al. 1992) in an idealized North Atlantic basin. In each model, two experiments are presented, one forced by anomalous wind stress, and the other by anomalous surface buoyancy (interfacial entrainment) forcing.

The QG model (Fig. 8) has a double-gyre mean circulation. The model parameters are $D_1 = 300$ m, $D_2 = 700$ m, $D_3 = 4000$ m, $g'_{12} = g'_{23} = 2$ cm s^{-2}, $f_0 = 0.73 \times 10^{-4}$ s^{-1}, $\beta = 2 \times 10^{-11}$ m^{-1} s^{-1}, biharmonic mixing coefficient 10^{10} m^4 s^{-1}, resolution 25 km $\times$ 25 km, and domain size 4000 km $\times$ 6000 km. The Ekman pumping is slightly asymmetrical with a meridional width of 2100 km and 1900 km for the subtropical and subpolar gyres, respectively. Figures 8a–c plot the case forced by a local Ekman pumping of a 3-yr period. The first mode of a 3-yr free wave has about 2 wavelengths across the basin. The SSH variability shows strong N-mode amplitude (Fig. 8a) that propagates westward rapidly as seen in the phase diagram (Fig. 8c). The A mode is visible but relatively weak and propagates southwestward slowly. The general pattern of the two wave rays agree well with the WKB analysis (appendix B, Fig. B1). In comparison to the SSH response in Fig. 8a, the upper thermocline temperature field (Fig. 8b) has a weaker signal in the N mode. Under entrainment forcing, however, the opposite occurs as shown in Figs. 8d–f. The A mode becomes dominant, especially in the upper thermocline temperature field (Fig. 8e), while the N mode is visible only in SSH (Fig. 8d).

The basic features in the QG model are reproduced in a 2.5-layer primitive equation model with realistic North Pacific geometry (Zhang 1998) (Fig. 9). The model is first spun up to the steady state under a mean wind field that resembles the observed annual mean wind field. Then a 10-yr periodic Ekman pumping anomaly is added in the midlatitudes of the central North Pacific (marked in Fig. 9c). The experiment is continued for another 80 years with the data of the last 60 years used for harmonic analyses (Figs. 9a–c). The SSH amplitude is dominated by a westward tongue all the way to the Kuroshio (Fig. 9a). The phase diagram further shows that this tongue reaches the western boundary in about 5 years (Fig. 9c). This is clearly the N mode. The A

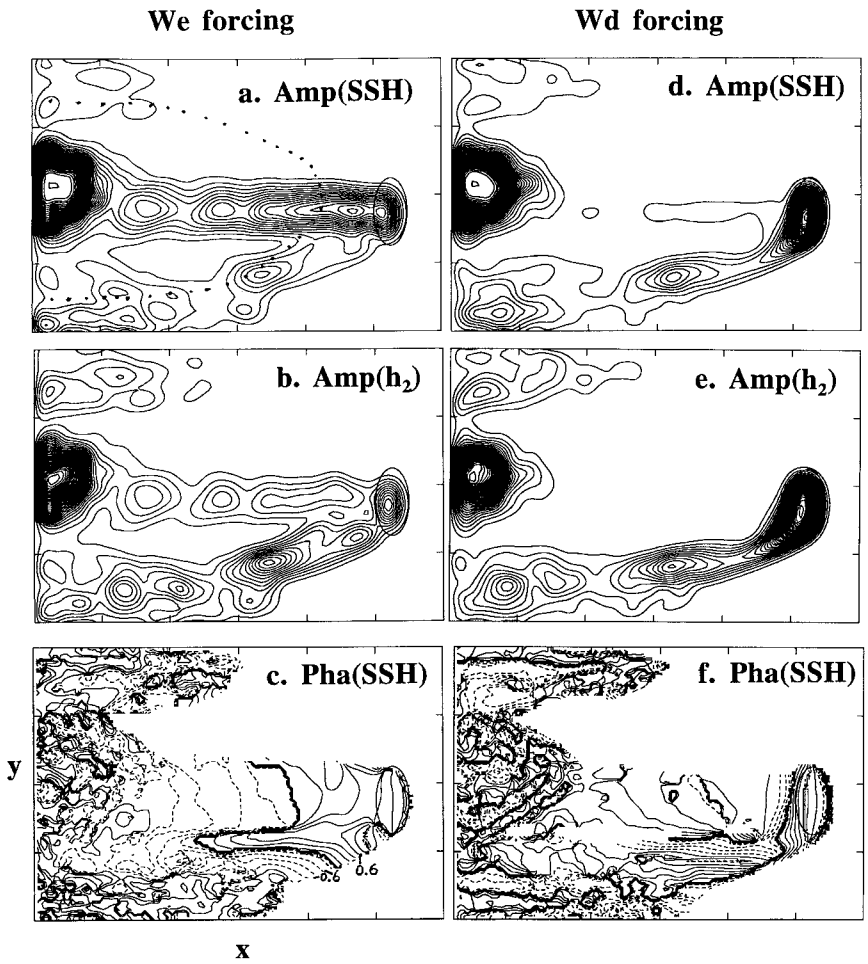

FIG. 8. Three-layer QG model experiments forced by 3-yr periodic, localized (elliptical) forcing. The mean circulation is a double-gyre circulation with the Rhines–Young pool indicated in (a) by the dotted line. The amplitude and phase of the 3-yr harmonic are plotted for two cases. The first case is forced by Ekman pumping (W_e). The response is shown for (a) the amplitude of SSH (ψ_1), (b) the upper thermocline temperature ($h_2 \sim \psi_2 - \psi_1$, and (c) the phase of SSH. The most striking feature is a dominant N mode that propagates westward and a weaker A mode that follows the gyre circulation. The second case is forced by entrainment forcing (W_d). The response is shown for (d) the amplitude of SSH, (e) the upper thermocline temperature, and (f) the phase of SSH. Now, the A mode becomes dominant. The contour interval is arbitrary for the amplitude and 0.3 yr for the phase.

mode has little signal in SSH (Fig. 9a) but becomes visible in the upper thermocline temperature field as a weak amplitude tongue that extends southwestward (Fig. 9b). The response under entrainment forcing (Figs. 9d–f) is in sharp contrast to that under wind forcing. With an anomalous entrainment forcing, the dominant signal in the upper thermocline temperature field (Fig. 9e) is a tongue of the A mode that first extends southward to about 20°N, and then extends southwestward toward western boundary at 15°N. The phase diagram (Fig. 9f) further shows that this wave path takes more than 10 years to reach the western boundary. The N-mode signal also appears as a weak amplitude tongue that extends westward in the SSH field (Fig. 9d).

The two models above, although relatively simple to understand, have several serious limitations. First, the vertical resolution is too coarse. Second, there is not a surface mixed layer. Third, surface buoyancy forcing anomaly is indirectly represented by an interfacial entrainment. To improve these aspects, a 13-layer MICOM model will be used. The model has a domain of 0° to 60° in longitude and 20°S to 60°N in latitude with a resolution of 2° in both longitude and latitude. There are 12 isopycnal layers and an active surface mixed layer. The surface wind stress forcing is the zonal mean Atlantic zonal wind stress; the surface temperature and salinity are restored toward the zonal mean Levitus (1982) SST and SSS with a restoring time of 90 days.

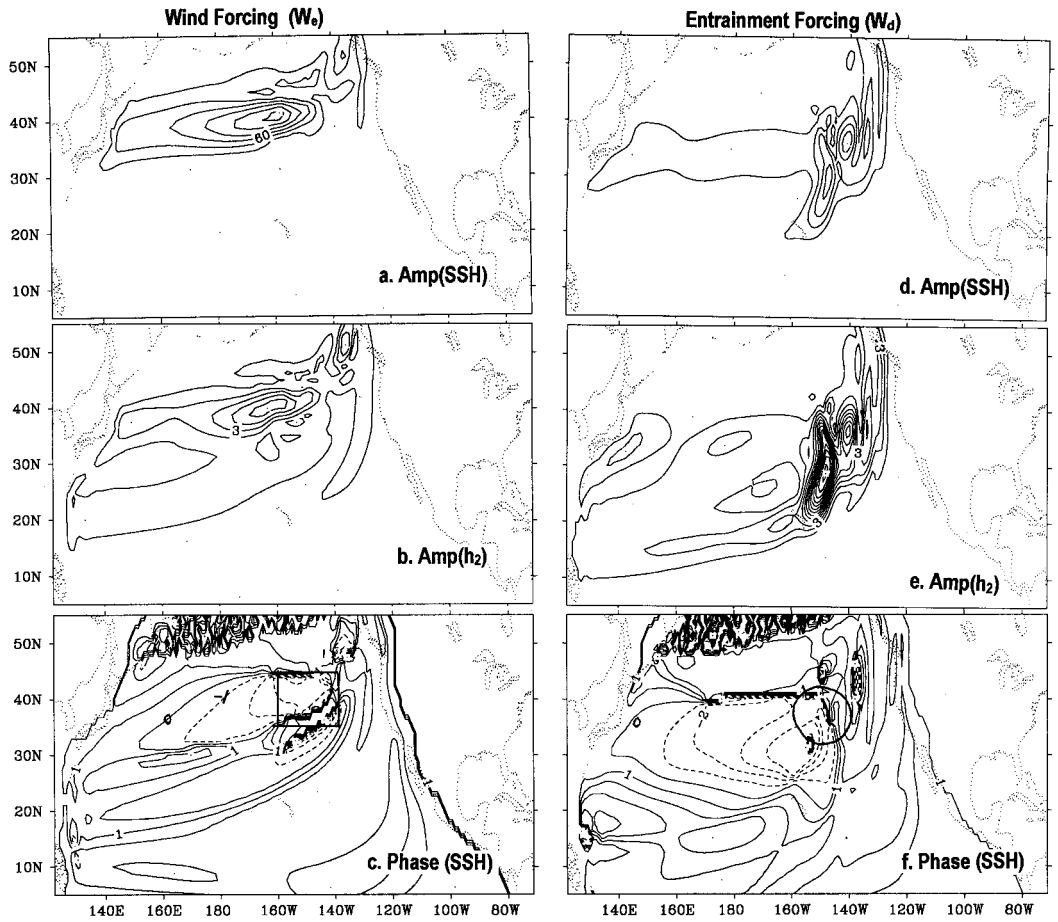

FIG. 9. Two experiments in a 2.5-layer primitive equation model with realistic Pacific geometry north of 30°S (only north of the equator is shown) (Zhang 1998). The model resolution is 1° × 1°. An annual mean zonal wind stress resembling the COADS wind is used to spin up the model to a steady state. Two experiments are then carried out under 10-yr periodic, localized, anomalous forcings: one for Ekman pumping forcing (a)–(c) and the other for entrainment forcing (d)–(f). The location of the forcings are marked in (c) and (f), at the center of which the magnitude of the anomalous forcing is about 10^{-6} m s^{-1} (Ekman pumping) for wind forcing and 10^{-5} m s^{-1} for entrainment forcing. The amplitude and phase of the 10-yr harmonic response are plotted. The amplitude of the sea surface pressure (equivalent to SSH here) is plotted in (a) and (d) (in 20 kg m^2 s^{-2}), the amplitude of the upper-layer thickness h_2 is plotted in (b) and (e) (in 1 m); the phase of the surface pressure is plotted in (c) and (f) (in 1 yr). The responses are similar to those in the QG experiments in Fig. 8.

A full annual cycle is used in both the wind stress and restoring SST and SSS. The model is first spun up for 30 years before the anomalous forcing is imposed.

Figures 10 and 11 present the anomalous annual mean response 10 yr after a steady anomalous wind stress forcing is imposed. The anomalous wind curl has a uniform positive curl within a disk centered at (45°N, 35°E) of a radius of 10°, but has no wind curl outside the disk[3] (see Fig. 10a and the caption). The barotropic streamfunction shows the zonally enlongated anomalous cyclonic gyre spanning between 25° and 45°N. The SST change is small (less than 0.5°C, not shown). The SSH field (Fig. 10c) is dominated by a negative westward extending tongue, which can also be identified as the westward tongue of negative isopycnal depth anomalies in the upper (Fig. 10d, $25.5\sigma_T$), middle (Fig. 10e, $26.25\sigma_T$), and lower (Fig. 10f, $27\sigma_T$) thermocline. The coherent vertical structure can also be observed in the deep cold temperature anomalies along the meridional section at $x = 22$°E (between 30° and 50°N in Fig. 11a) and the zonal section at $y = 37$°N (west of 40° in Fig. 11b). These features are consistent with the N-mode structure. [Notice that the positive temperature (or depth) anomaly near the eastern boundary in the middle latitude is caused by the strong Ekman downwelling forced by the anomalous meridional wind stress along the eastern boundary (see Fig. 10a).] In addition to the deep, westward N-mode anomaly, a shallow cold tem-

[3] This wind anomaly pattern is designed by T. Inui and A. Kubokawa.

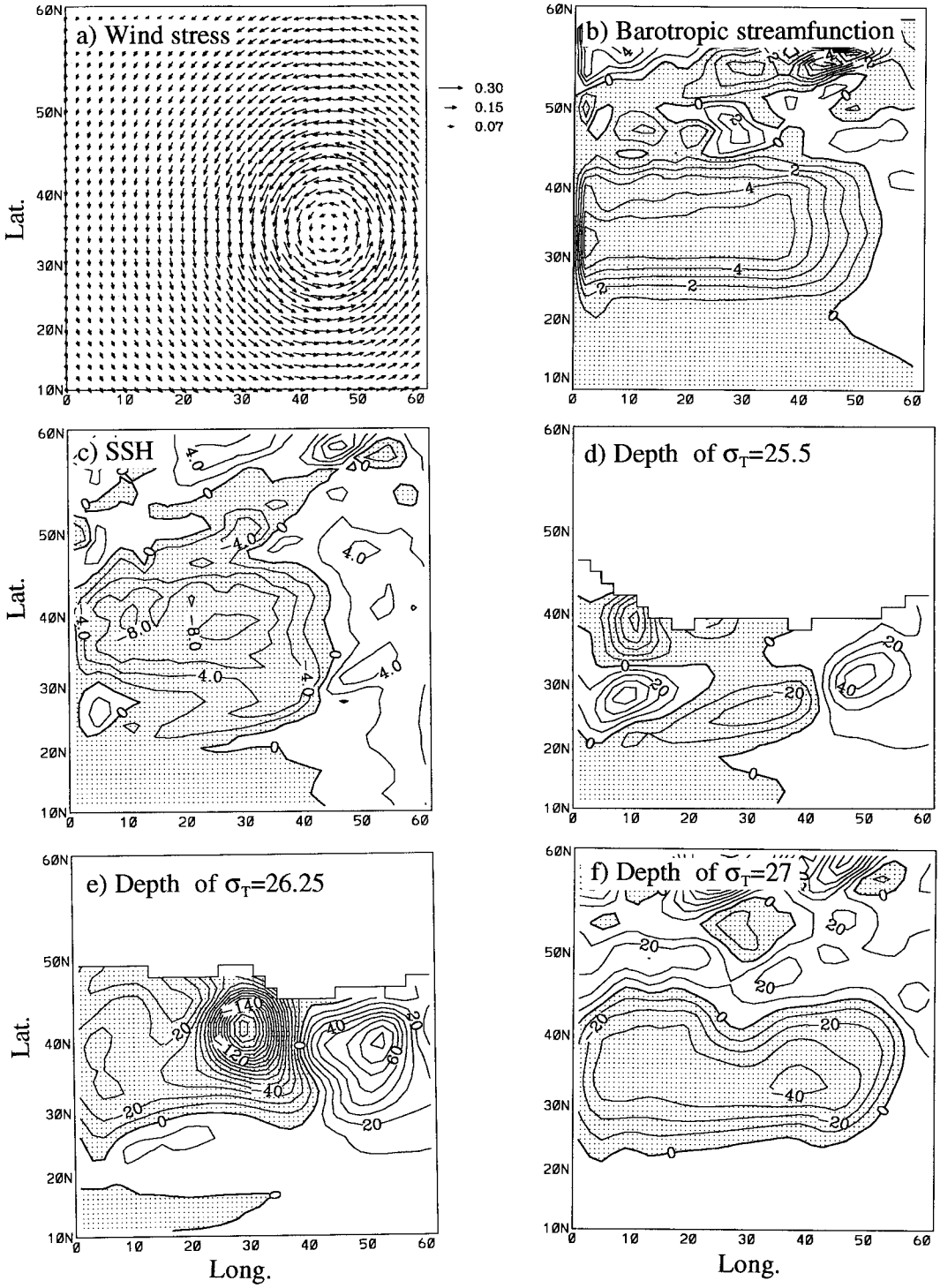

FIG. 10. The anomalous annual mean response of MICOM to a steady wind stress curl anomaly (10 yr after the anomalous forcing). The model has a horizontal resolution of 2° and 13 layers (mixed layer, $22\sigma_T$, $23\sigma_T$, $24\sigma_T$, $25\sigma_T$, $25.5\sigma_T$, $26\sigma_T$, $26.25\sigma_T$, $26.5\sigma_T$, $27\sigma_T$, $27.45\sigma_T$, $27.6\sigma_T$, and $27.7\sigma_T$). The model climatology is forced by the zonal mean Atlantic zonal wind stress annual cycle and is restored toward the zonal mean surface temperature and salinity annual cycle (Levitus 1982) with a restoring time of 90 days. The anomalous wind stress varies with longitude (x) and latitude (y) as $(\Delta\tau_x, \Delta\tau_y) = (-y, x)\tau_0/r_0$ for $r \le r_0$, and $(\Delta\tau_x, \Delta\tau_y) = (-yr_0, xr_0)\tau_0/r^2$ for $r > r_0$. The wind stress anomaly in (a) has $\tau_0 = 0.3$ dyn/cm^2, $r^2 = (x - 45°)^2 + (y - 35°)^2$, and $r_0 = 10°$. (b) Barotropic streamfunction anomaly (CI = 1 Sv), (c) SSH anomaly (CI = 0.2 cm), (d) depth anomaly of the $25.5\sigma_T$, (e) depth anomaly of $26.25\sigma_T$, and (f) depth anomaly of $27\sigma_T$ [(CI = 10 m in (d)–(f)]. Shaded regions are negative values.

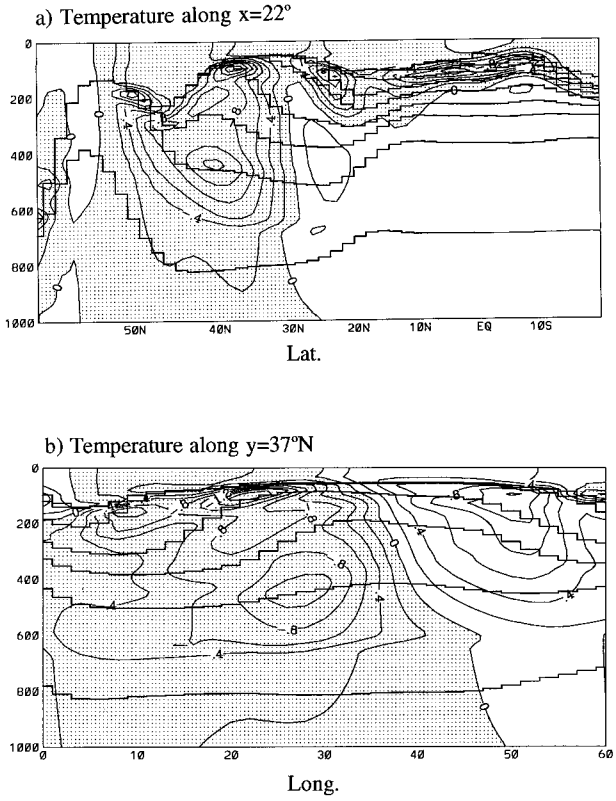

FIG. 11. Same run as in Fig. 10, but for temperature anomalies along (a) the meridional section at $x = 22°$ and (b) the zonal section at $y = 37°$N. Contour interval is 0.2°C, and the shaded region is negative.

perature anomaly follows the subduction flow and extends from the forcing region southwestward, as shown in the SSH (Fig. 10c), the upper thermocline (Fig. 10d), and the meridional temperature field (Fig. 11a). The vertical structure of this shallow anomaly resembles that of the A mode because it has its maximum in the upper thermocline and has a deep temperature anomaly out of phase with the upper layer. The magnitude of this A mode is, however, weaker than that of the deep N mode. This is similar to the QG and 2.5-layer model experiments (Figs. 8a–c, 9a–c). In all the cases, the wind stress curl anomaly forces predominantly the N-mode response, but also forces a significant A-mode response.

In contrast, Figs. 12 and 13 show the anomalous thermocline response to a cold surface forcing anomaly. The cold Gaussian shape restoring SST anomaly is localized in the region of 30° to 50°E, 30° to 40°N with a maximum of 2°C. The resulted anomalous SST has a maximum of about 1.8°C (Fig. 12a). Different from the wind curl forcing case, the dominant signal in the subtropical gyre is a southwestward extending advective signal in all the anomaly fields including the negative SSH (Fig. 12b), negative upper thermocline depth ($26\sigma_T$, Fig. 12c), and the positive deep thermocline depth ($27\sigma_T$, Fig. 12d). The lower thermocline temperature anomaly tends to be weaker and out of phase with the upper thermocline temperature. This baroclinic vertical structure can be observed by comparing the negative upper thermocline anomaly in Fig. 12c with the positive lower thermocline anomaly in Fig. 12d and can also be seen clearly in the meridional section at $x = 22°$E (Fig. 13a) and the zonal section at $y = 23°$N (Fig. 13b). This advective anomaly resembles closely to the A-mode structure in our theory, and the subduction resembles closely the observed North Pacific subduction anomaly (Deser et al. 1996; Zhang and Liu 1999, hereafter ZL; Schneider et al. 1998). Therefore, the surface cooling produces predominantly the A-mode response. This is consistent with our theory, the QG experiment (Figs. 8d–f) and the 2.5-layer model experiment (Figs. 9d–f).

Similar sensitivity experiments are also carrried out in the GFDL MOM1 model with a horizontal resolution of $1° \times 1°$. The wind curl forcing case is similar to the MICOM simulation. However, the cooling experiment produces a much weaker advective signal, probably due to the strong diapycnal diffusion in the model. Overall, our numerical experiments strongly support our WKB analyses in section 3 and section 4 as well as our speculative synthesis at the end of section 4.

6. Advective mode or passive tracer

The A mode shows some similarity to a passive tracer. A passive tracer in the subsurface will follow the subsurface flow perfectly (in the absence of diffusion). The A mode, as discussed above, tends to follow the circulation and, therefore, resembles a passive tracer. More specifically, in a ventilated zone, the wave path of an A mode follows closely to that of the subsurface ventilation flow path $\boldsymbol{U}_2$ (Figs. 1b,d and 2a). Moreover, in a Rhines–Young pool where the subsurface PV is homogeneous (Rhines and Young 1982), the A mode propagates as a perfect passive tracer, following the subsurface flow trajectory of $\boldsymbol{U}_2$ exactly [see (B.1) and appendix B].

In spite of some apparent similarity, it is more advantageous to treat the A mode as a dynamic mode, instead of a passive tracer. First as seen in section 4, the A mode has a distinct dynamic response to surface forcing: the A mode is most efficiently excited by surface buoyancy forcing. This forcing mechanism can only be understood by considering the dynamic nature of the A mode, rather than treating it as a passive tracer.

There are also important differences between the propagation of the A mode and a passive tracer. One obvious difference has been discussed in section 2. In a shadow zone where no mean subsurface flow exists, a passive tracer would remain at its initial position, while the A mode propagates along the wave characteristics (Figs. 1b, 3a).

The ventilated zone is more interesting and subtle. Here, the speed of the A mode propagation could be

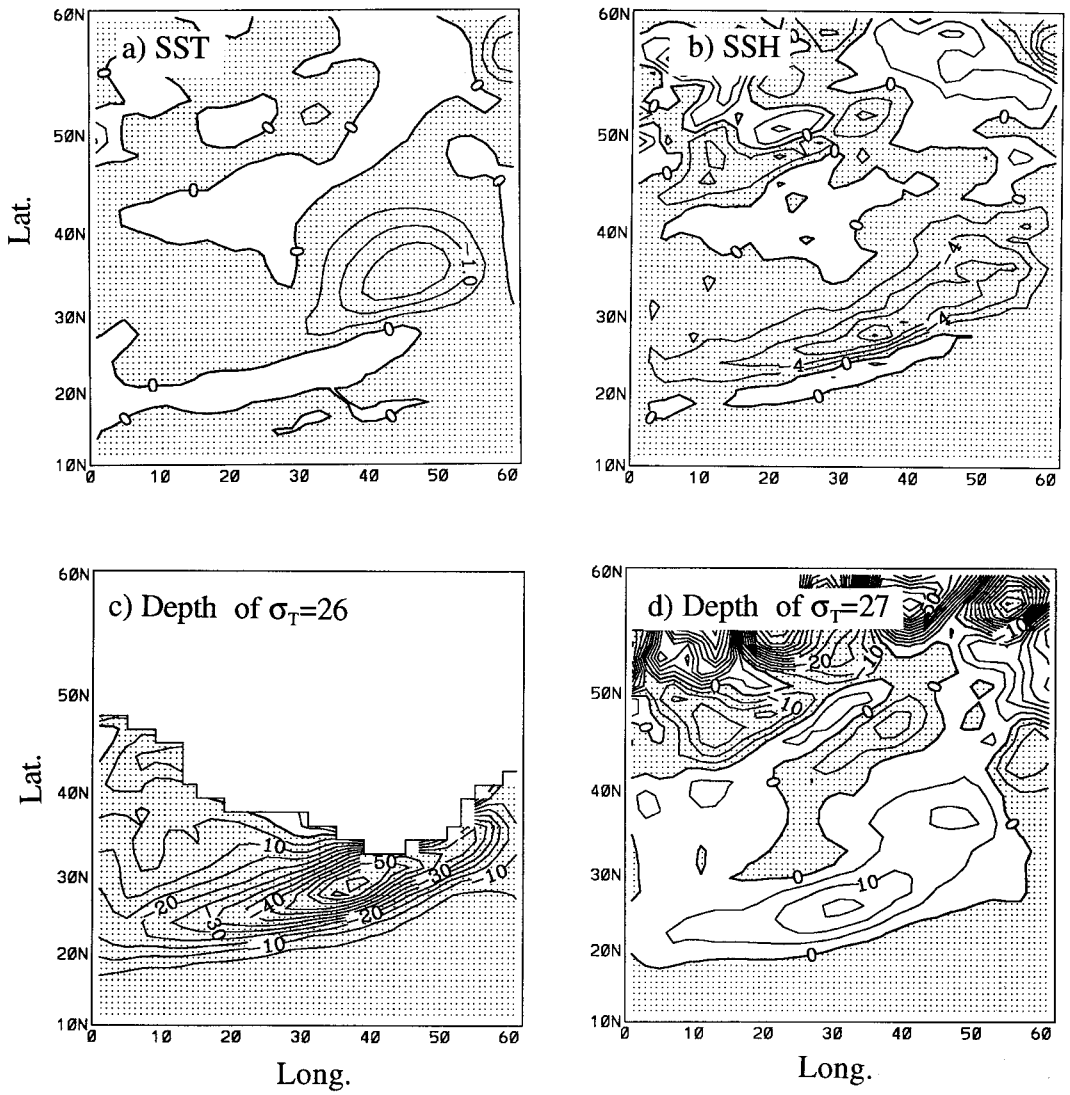

FIG. 12. The anomalous March response of MICOM to a steady surface cooling anomaly (20 years after the cooling). (a) SST anomaly (CI = 0.5°C), (b) SSH anomaly (CI = 2 cm), (c) depth anomaly of $26\sigma_T$, and (d) depth anomaly of $27\sigma_T$ [(CI = 5 m in (c) and (d)].

substantially slower than that of the subduction flow $\boldsymbol{U}_2$, in spite of similar propagation directions. This can be seen by comparing the wave rays with the corresponding flow trajectories in the subsurface as shown in Fig. 1. After a total traveling time of $t = 8.6$, none of the A-mode wave rays that start in the ventilated zone have reached the western boundary (Fig. 1b). However, all of the subsurface ventilation flow trajectories have passed the western boundary (Fig. 1d). Indeed, the speed of the A-mode wave ray seems to be close to that of the wave characteristics shown in Fig. 1f, both being slower than the subsurface flow in Fig. 1d; that is,

$$|(U_2, V_2)| > |(U_B - d_1 d_2, V_B)| \geq |(C_{gxA}, C_{gyA})| \quad (6.1)$$

in the ventilated zone. This relationship also seems to hold in more general cases, although we have failed to find a general proof analytically. Some insight can be gained on (6.1) as follows: on the one hand, one can show in the 2.5-layer QG ventilated thermocline model solution that

$$(U_2, V_2) = (U_B - d_1 d_2, V_B)/d_2 \quad (6.2)$$

in the ventilated zone. Since $d_2 < 1$, the ventilation flow is always parallel to, but faster than, the wave characteristics. For a typical thermocline stratification of $d_2 \approx 0.5$, the ventilation flow is about twice as fast as the wave characteristics. On the other hand, in the limit of a 2-layer thermocline (which can be achieved in a 2.5-layer model by increasing the stratification at the bottom of the thermocline), the second mode has the same speed as the wave characteristics (Rhines 1986; Dewar 1989; Liu 1996):

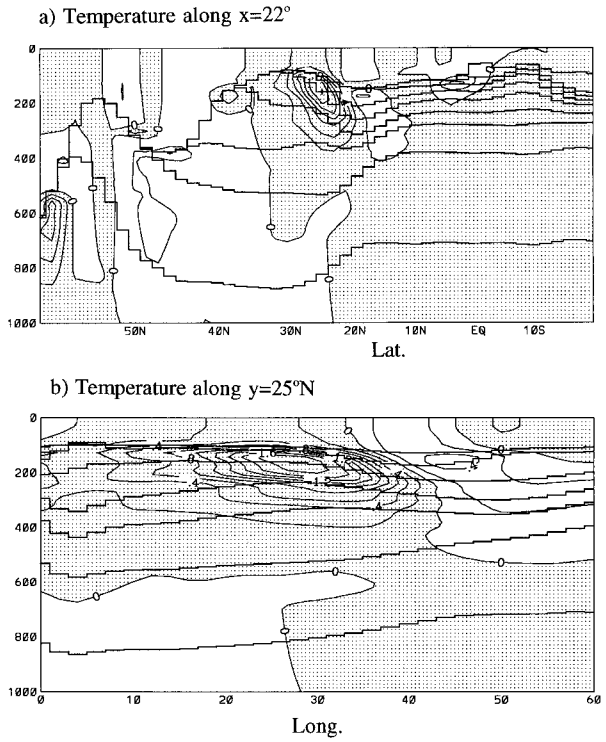

FIG. 13. Same run as in Fig. 12 but for temperature anomalies along (a) the meridional section at $x = 22°$ and (b) the zonal section at $y = 25°$N. Contour interval is 0.2°C, and the shaded region is negative.

$$(U_B - d_1 d_2,\ V_B) = (C_{gxA},\ C_{gyA}). \qquad (6.3)$$

This suggests that the speed of the wave characteristics may not be much different from that of the A mode. Hence, the combination of (6.2) and (6.3) suggests that the A-mode wave ray should be slower than the ventilation flow. For a typical thermocline structure $d_2 \approx 0.5$, the speed of the A-mode wave ray may be less than half that of the ventilation flow. In the 2.5-layer model, we have been unable to find a general proof of the A-mode speed. However, in the low-frequency limit, as discussed regarding (3.10a), we have $(C_{gxA}, C_{gyA}) = (U_B - d_1 d_2, V_B)/(1 + d_1)$. Thus, the A-mode speed is somewhat slower than the wave characteristic, which in turn is slower than the second-layer ventilation flow.

The wave amplitude could also differ significantly between the A mode and a passive tracer. One example is the planetary wave instability found in the southwestern part of a subtropical gyre (Liu 1998), where the A mode is destabilized by coupling with the N mode. This may imply an amplification of the wave amplitude during propagation.[4] A passive tracer, in contrast, can never become unstable and therefore its magnitude can never exceed its initial value. Finally, even in the stable region, the amplitude of the A mode, which varies according to the dynamics, may be substantially different from that of a passive tracer. This issue remains to be studied in the future.

7. Summary and discussion

The response of a thermocline gyre to surface wind and buoyancy forcing was studied with the WKB method in a 2.5-layer QG model. The theory is substantiated by numerical experiments. A unified theory is proposed for the planetary waves in the thermocline. Ekman pumping is the most efficient mechanism to generate the N mode, which has its clearest signal in the SSH field and the lower thermocline. This mode propagates westward rapidly even in the presence of a gyre circulation, because of the non-Doppler-shift effect. In contrast, surface buoyancy forcing generates the strongest response in the A mode, with its largest signature in the upper thermocline temperature field. This mode is strongly advected by the subsurface gyre circulation, but may propagate at a different speed in the central to eastern part of the gyre where it is dominated by the ventilated zone and the shadow zone.

a. Different wave pathways

Our theory seems to be consistent with the interannual to decadal variability recently observed in the North Pacific. The observed SSH field seems to exhibit a dominant westward propagation at all latitudes (Jacobs et al. 1994; Chelton and Schlax 1996). Similar westward propagation has also been found recently for decadal temperature variability in the lower thermocline in the historical upper-ocean data (Zhang and Levitus 1997; Miller et al. 1998; ZL; White and Cayan 1997, manuscript submitted to *J. Geophys. Res.*, hereafter WC). This propagation, according to our theory, may be mainly forced by the wind-stress curl forcing, most likely along the eastern boundary. The variable wind stress curl excites the N mode, which has the strongest amplitude at the SSH and the bottom of thermocline (also see Liu 1998) and propagates westward across the Pacific. This is consistent with a model study of Miller et al. (1998). In the meantime, the upper thermocline temperature variability (Deser et al. 1996; Zhang and Levitus 1996; WC; ZL; Schneider et al. 1998) seems to follow a subduction circulation path. This, according to our theory, may be caused mainly by surface buoyancy forcing, which tends to excite the A mode. In the case of steady-state forcing (zero frequency), this forcing mechanism of the subduction temperature anomaly is supported by a recent study of the North Pacific thermocline anomaly by Schneider et al. (1998) in light of the dynamics of the ventilated thermocline, and by a theoretical study with idealized ventilated thermocline

[4] The ray tracing in the instability region is no longer valid formally. The unstable region, however, only covers a small area in the southwest corner in the example of Fig. 1b.

by Huang and Pedlosky (1998). Finally, the coexistence and the three-dimensional structure of the two types of propagation pathways have been identified recently in the observed thermocline, confirming our theoretical prediction here (ZL).

Substantial interannual variability has been found in Bermuda in SSH (Sturges and Hong 1995), temperature, and salinity (Joyce and Robbins 1996). The interannual variability of SSH in Bermuda can be predicted successfully by integrating the forced response of the first baroclinic mode from the eastern boundary along the same latitude. The same technique, however, is not successful in the simulation of the upper thermocline temperature variability. This may be understood in our theory as follows. The SSH variability is dominated by the N mode, which propagates predominantly westward. The N mode should also produce a significant change in the lower thermocline. This is consistent with Joyce and Robbins (1996) in that the interannual SSH variability is mostly due to temperature and salinity changes in the lower thermocline (depth 500–1000 m). In contrast, upper thermocline temperature involves higher modes, which, among other things, could be advected from upstream in the north. Integration from the east can capture most of the influence from the N mode, but not the A mode. The former applies the best to the SSH and the lower-thermocline temperature, while the latter applies best to upper-thermocline temperature.

b. The A mode

Previous studies have shown that the A mode plays a fundamental role in the formation of the mean thermocline circulation, notably the different dynamic zones (Luyten and Stommel 1986; Liu 1993a). It has also been implied that the A mode also plays an important role for thermocline variability (Rhines 1986; Dewar 1989; Liu 1993b, 1996; Liu and Pedlosky 1994). The contribution of the present work (and Liu 1998), however, is to distinguish the A mode from other planetary wave modes, especially the N mode. This distinction may enable us to understand the entire spectrum of upper-ocean variability from a unified point of view.

Our theory suggests that the propagation speed of the A mode is slower than a passive tracer in the ventilated zone, the same as a passive tracer in the pool (appendix B), and faster than the passive tracer in the shadow zone. This complex relationship remains to be studied. A crude examination from available observations seems to support our theory, at least in the ventilated zone: the observed propagation speed is somewhat slower than the subduction current speed. In Deser et al. (1996, their Fig. 16), the decadal temperature anomaly patch moved southward about 900 km in 10 years, corresponding to a southward propagation speed of about 0.3 cm s^{-1}. This speed is about half that of the mean current speed, which is about 0.7 cm s^{-1} according to a recent estimate of Schneider et al. (1998). In a further isopycnal analysis by Schneider et al. (1998, their Fig. 6), one can also identify a propagation speed slower than the mean current speed, especially in the northern part (north of 26°N) and the very southern part (south of 21°N) of the subtropical gyre. However, in the central part, the propagation speed seems to be close to the current speed. A more careful study is needed in both observations and theory to clarify the propagation speed of the subduction anomaly.

c. Relevance to climate variability

Our study may also help us to understand decadal climate variability in the coupled ocean–atmosphere system. One prominent example is in the North Pacific, where two competing hypotheses for decadal climate variability have been proposed recently. Latif and Barnett (1994) suggest a decadal variability whose memory comes from the westward propagation of Rossby waves within the subtropics. In contrast, Gu and Philander (1997) proposed a decadal oscillation mechanism whose long time delay originates from the equatorward subduction of a thermal anomaly in the midlatitudes (Liu et al. 1994; McCreary and Lu 1994). This equatorward subduction—an oceanic teleconnection bridge, is analogous to the atmospheric PNA teleconnection bridge that plays a critical role in tropical–extratropical interaction (Wallace and Gutzler 1981; Lau and Nath 1996). As far as the oceanic thermocline is concerned, the Latif and Barnett mechanism may depend more on the N mode, which propagates westward and has a strong signature in SSH (and in turn surface geostrophic currents). The Gu and Philander mechanism may depend upon the A mode that follows the subduction circulation and has a strong signature in the subsurface temperature field. The N mode is likely to be forced predominantly by wind-stress curl forcing, while the A mode is mainly generated by surface diabatic forcing. Excitation of various oceanic modes by different forcing mechanisms may give rise to diverse decadal climate variability in a coupled system.

Acknowledgments. I have enjoyed discussions of numerical model experiments with Dr. S. Borisov (QG model), Mr. Liping Zhang (2.5-layer model), Mr. Shin Shangik (MICOM), and Dr. T. Inui (MOM1). Comments from two reviewers are greatly appreciated. The editorial assistance of Ms. Kennedy is of great help. This work is supported by NSF, NOAA, and ONR.

APPENDIX A

Forced Response in a Motionless Basic State

In the absence of a mean flow, the local response can be derived from (4.3) as

$$\phi_{1N} = -[(1 - 2a_A)w_e + a_A w_d]/(a_N - a_A),$$

$$\phi_{1A} = -[(1 - 2a_N)w_e + a_N w_d]/(a_A - a_N), \quad \text{(A.1)}$$

TABLE A1. Local response ($W_e = 0$, $m = 0$)

Ratio/forcing	w_e forcing ($w_d = 0$)	w_d forcing ($w_e = 0$)
h_{1N}/h_{1A} (or ϕ_{1N}/ϕ_{1A})	$-a_A k_A/a_N k_N > 1$*	$0 > a_A/a_N$**
h_{2N}/h_{2A} (or q_{1N}/q_{1A})	$0 < -a_A/a_N$**	$0 > a_A k_N/a_N k_A > -1$
ϕ_{2N}/ϕ_{2A}	$-k_A/k_N < -1$	-1
q_{2N}/q_{2A}	-1	$0 < k_N/k_A < 1$
E_N/E_A***	$\frac{(d_1 k_N)^2 + (\omega a_N)^2}{(d_1 k_A)^2 + (\omega a_A)^2} \times \left(\frac{a_A k_A}{a_N k_N}\right)^2 > 1$*	$\frac{(d_1 k_N)^2 + (\omega a_N)^2}{(d_1 k_A)^2 + (\omega a_A)^2} \times \left(\frac{a_A}{a_N}\right)^2 < 1$*

* Unless $2d_1 \ll d_2$.
** $|a_N/a_A| \geq 1$ for $d_2 \geq 2d_1$; $|a_N/a_A| < 1$ for $d_2 < 2d_1$,
*** Planetary wave energy in the 2.5-layer model $E = [(\phi_2 - \phi_1)^2 + \phi_2^2]/2$.

where, for simplicity, the forcing has been assumed zonally uniform $m = 0$. The zonal wavenumbers for the two dynamic modes can be derived from (3.3a,b) as

$$k_A^N = \omega[-(1 + d_1) \pm \Delta]/2d_1 d_2, \qquad \text{(A.2)}$$

where $\Delta = [(1 + d_1)^2 - 4d_1 d_2]^{1/2} \equiv (d_2^2 + 4d_1^2)^{1/2}$. Therefore, we have

$$k_A < k_N < 0. \qquad \text{(A.3)}$$

Furthermore, with the aid of (3.4) and (A.3), the wave structure can be shown to satisfy

$$a_N > 0 > a_A, \qquad \text{(A.4)}$$

and

$$|a_N/a_A| > |k_N/k_A| < 1; \qquad \text{(A.5)}$$

$$|a_N/a_A| \geq 1 \quad \text{for } d_2 \geq 2d_1;$$

$$|a_N/a_A| < 1 \quad \text{for } d_2 < 2d_1, \qquad \text{(A.6)}$$

Equation (A.3) states that the N mode has a larger scale and therefore propagates westward faster than the A mode. Equation (A.4) shows that the flows in the two layers are in the same direction for the N mode, but in the opposite direction for the A mode.

With the aid of (A.1)–(A.6), the modal response can be obtained as in Table A1. The point is the Ekman pumping forcing is efficient in generating a strong SSH signal in the *N* mode, while the entrainment forcing is efficient in generating a strong upper-thermocline temperature anomaly in the A mode. This has also been shown to be valid for a more general thermocline in section 4 (Figs. 5 and 6). Finally, the solution here also applies to the shadow zone under a spatially uniform Ekman pumping $W_e(y) = W_0$ and spatially uniform perturbation forcings ($m = n = 0$). Therefore, the major features here also apply approximately to a shadow zone.

APPENDIX B

Forced Response in the Rhines–Young Pool

In the Rhines–Young pool (Rhines and Young 1982), the PV is homogeneous in layer 2. Under Ekman pumping $W_e(x, y)$, the mean flow field in our 2.5-layer model (2.1) can be derived to satisfy

$$d_1\Phi_1 + d_2\Phi_2 = \Phi_B = \int_{xE}^{x} W_e(x, y)\, dx,$$

$$\Phi_2 = (d_1 d_2 y + \Phi_B)/(1 + d_1).$$

The wave rays in the pool, under general forcing (3.1), can be derived from (3.3) as

$$k_N = -\omega/(1 + d_1), \qquad k_A = (\omega - nV_2)/U_2. \qquad \text{(B.1)}$$

Thus, the N mode radiates purely westward. The speed, $C_{gxN} = -(1 + d_1)$, is the planetary wave speed in the 1.5-layer thermocline model that combines layers 1 and 2 [see Eq. (2.3) of Liu (1998)]. In contrast, the group velocity of the A mode satisfies

$$(C_{gxA}, C_{gxA}) = (U_2, V_2) = (U_B - d_1 d_2, V_B)/(1 + d_1),$$

and therefore is purely advected by the layer-2 mean flow, both being parallel to, but slower than, the wave characteristics. Figure B1 shows wave rays similar to that of Fig. 3 but in a double-gyre that has a Rhines–Young pool in the midlatitudes. It is seen that the N mode (Fig. B1a) propagates westward regardless of the mean flow. The A mode, however, tends to follow the gyre circulation. Within the pool, the A mode follows exactly the mean flow of layer 2. In most of the shadow zone, the A mode follows approximately ($U_B - d_1 d_2$, V_B), as discussed in Figs. 1–4 and later in appendix C.

Now, we turn to the forced modal response in the pool. For simplicity, the perturbation forcing is assumed to be spatially uniform $m = n = 0$. First, with (2.6) and (B.1), the module structure can be derived as

$$a_N = 0.5, \qquad a_A = -d_1/(U_1 - U_2). \qquad \text{(B.2)}$$

Therefore, the N mode has an equivalent barotropic structure with upper-layer flow twice the strength of the lower-layer flow. In contrast, the A mode usually has the two layers flowing in the opposite direction except in the region of strong westward flow with $U_1 - U_2 < 0$, which may occur in the southern part of the subtropical gyre.

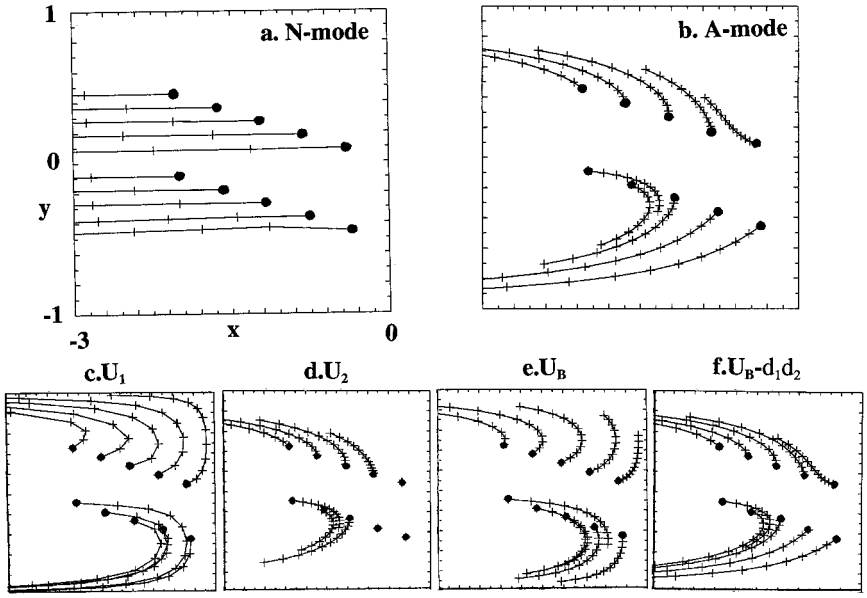

FIG. B1. As in Fig. 1 but in a double-gyre circulation with the Rhines–Young pool in appendix B. Now $W_e(y) = W_{e0}\sin(y\pi)$, where $W_{e0} = 0.15$. The time interval between each pair of marks is 0.4.

Finally, the modal projections are derived from (4.2)–(4.3) and (B.2) as

$$\phi_{1N} = \frac{i\omega[-(u_1 - u_2 + 2d_1)w_e + d_1 w_d]}{A(\omega, 0, 0)(a_N - a_A)(u_1 - u_2)},$$

$$\phi_{1A} = \frac{-i\omega w_d}{2A(\omega, 0, 0)(a_A - a_N)}. \qquad \text{(B.3)}$$

Anomalous Ekman pumping only forces the N mode and therefore generates little variability in the upper thermocline temperature. The failure of the Ekman pumping to force the A mode, and in turn a strong upper thermocline temperature variability, can be understood similarly as Liu (1996). Since the A mode is dominated by advection process, an anomalous Ekman pumping quickly generates a horizontal Sverdrup flow (after the passing of the fast N mode), with which the associated temperature advection tends to cancel the vertical advection effect due to Ekman pumping. In contrast, w_d forces response in both modes. Nevertheless, from the modal response to w_d forcing

$$h_{1N}/h_{1A} = 2d_1/(U_1 - U_2),$$
$$h_{2N}/h_{2A} = -d_1/(1 + U_2), \qquad \text{(B.4)}$$

we see that buoyancy forcing generates a dominant response in the thermocline temperature field h_2 in the A mode, unless it is in the region where the westward flow is too strong.

APPENDIX C

Wave Rays in a Ventilated Thermocline

Here, we derive the wave rays for a QG ventilated thermocline, forced by spatially uniform Ekman pumping $W_e(y) = W_0 < 0$. The thermocline solution south of the outcrop line $y = y_0$ is derived as (Hendershoot 1989)

$$\Phi_1 = -d_2 y, \qquad \Phi_2 = [d_1 d_2 y + xW_0]/d_2$$

for $x < x_S(y)$, in the ventilated zone and

$$\Phi_1 = -xW_0/d_1, \qquad \Phi_2 = 0$$

for $x_S(y) < x < 0$ in the shadow zone. Here $x_E = 0$ is the eastern boundary, and

$$x_S(y) = d_1 d_2 (y_0 - y)/W_e(y)$$

is the shadow zone boundary (caption, Fig. 1). Now since the mean flow does not vary with space within the ventilated zone or the shadow zone, both wavenumbers should remain unchanged at their initial values as in (3.6). For simplicity, we only present the case of $n = 0$. The wave rays are derived following (3.5), while the wave structure are derived from (2.6). In the ventilated zone,

$$k_A^N = [-(1 + 2d_1) \pm \Delta]\omega/2d_1 d_2, \qquad \text{(C.1)}$$

where $\Delta = [(1 + 2d_1)^2 - 4\, d_1 d_2]^{1/2} \equiv [1 + 2(2d_1)^2]^{1/2}$. We then have

$$\dot{x}_A^N = \frac{-2d_1d_2}{1 + 2d_1 \mp \Delta}, \qquad \dot{y}_A^N = \frac{W_0(\Delta \mp 1)}{1 + 2d_1 \mp \Delta},$$

$$a_A^N = -\frac{d_1[\pm\Delta - (1 + 2d_1)]}{d_2(\Delta - 1)}. \tag{C.2}$$

In the shadow zone,

$$k_A^N = [-(1 + d_1) \pm \Delta]\omega/2d_1d_2, \tag{C.3}$$

where $\Delta = [(1 + d_1)^2 - 4d_1d_2]^{1/2} \equiv [d_2^2 + (2d_1)^2]^{1/2}$. We then have

$$\dot{x}_A^N = -\frac{\pm 2d_1d_2}{\pm(1 + d_1) - \Delta}, \qquad \dot{y}_A^N = \mp\frac{W_0}{\Delta},$$

$$a_A^N = -\frac{d_1[\pm\Delta - (1 + d_1)]}{d_2(\Delta - d_2)}. \tag{C.4}$$

The wave rays in (C.2) and (C.4) are independent of the forcing frequency. In a more general thermocline (e.g., Fig. 4), the wave rays may vary with frequency, although not significantly. Furthermore, with (C.1)–(C.4), one can prove that

1) $a_N > 0$, $a_A < 0$ in both zones; the N mode and the A mode retain the structure of the first and second modes, respectively.
2) $\dot{x}_N < \dot{x}_A < 0$ in both zones; the N mode is always more westward than the A mode.
3) In a subtropical gyre where $W_0 < 0$, we have $\dot{y}_A < 0$, $\dot{y}_N < 0$ in the ventilated zone, but $\dot{y}_A < 0$, $\dot{y}_N > 0$ in the shadow zone. Thus, although both waves propagate southward over most of the ocean, the N mode propagates northward in the shadow zone (see Figs. 1, 3, and B1).
4) For the A mode, the direction of the wave ray relative to the characteristics $(U_b - d_1d_2, V_b) = (-d_1d_2, W_0)$ is

$$0 < \frac{dy}{dx}\Big/\frac{V_b}{U_b - d_1d_2} = \frac{1}{2}\left(1 + \frac{1}{\sqrt{1 + 2(2d_1)^2}}\right) < 1$$

in the ventilated zone (C.5)

and

$$\frac{dy}{dx}\Big/\frac{V_b}{U_b - d_1d_2} = \frac{1}{2}\left(1 + \frac{1 + d_1}{\sqrt{(1 + d_1)^2 - 4d_1d_2}}\right) > 1$$

in the shadow zone. (C.6)

Here we have used the wave ray slope as $dy/dx = \dot{y}/\dot{x}$. The A-mode wave ray always follows closely to $(U_B - d_1d_2, V_B)$. According to (C.5) and (C.6), both of them are always in the same quadrant. The wave ray has a slightly smaller slope in the ventilated zone, but a larger slope in the shadow zone. For a typical thermocline of $d_1 = 0.3$ to 0.5, the slope difference can be shown to be within 10%–20% in both zones; d_1 vanishes, they coincide with each other. These features have also been seen in the more general thermocline case in Figs. 1–4.

APPENDIX D

Planetary Wave Rays in a 3.5-Layer Thermocline

Wave ray solutions in the 2.5-layer model (section 2 and 3) can be extended to a 3.5-layer model. Assuming the density for layers 1, 2, 3, and 4 as $\rho - 3\Delta\rho$, $\rho - 2\Delta\rho$, $\rho - \Delta\rho$, and ρ, respectively, the 3.5-layer QG PV equations are

$$[\partial_t + J(\psi_n,)]q_n = 0 \quad \text{for} \quad n = 1, 2, 3.$$

Here, $q_1 = \beta y + (\psi_2 - \psi_1)/L_D^2d_1$, $q_2 = \beta y + (\psi_3 - 2\psi_2 + \psi_1)/L_D^2d_2$, $q_3 = \beta y + (\psi_2 - 2\psi_3)/L_D^2d_3$, where $L_D^2 = g'D/f^2$, $g' = g\Delta\rho/\rho$, $D = D_1 + D_2 + D_3$, and D_n and $d_n = D_n/D$ are the dimensional and dimensionless mean layer thicknesses for layer n. The equations can be linearized on mean flows (U_n, V_n) and the WKB solutions can be derived similar to that in the 2.5-layer model.

In the following, all variables will be nondimensionlized. The horizontal spatial scale, velocity, and time will be normalized by L, C, and L/C, respectively, where L is the basin scale and $C = \beta L_D^2$. For perturbations of the form $\phi_n e^{i(kx+ly-\sigma t)}$, the eigenvalue equation can be derived as

$$\sigma^3 + c_2\sigma^2 + c_1\sigma + c_0 = 0. \tag{D.1}$$

Here

$$c_2 = 2 + (d_1 - d_3)k - R_2 - R_3, \tag{D.2a}$$

$$c_1 = R_2(R_3 - k) - k[2R_B + (d_1 - d_3)R_3] + k^2[2d_1(d_2 + d_3) + d_2d_3], \tag{D.2b}$$

$$c_0 = k\{R_2R_B - k[d_2R_2(d_1 + d_3) + d_1d_3(R_1 + R_3)] + k^2d_1d_2d_3\}, \tag{D.2c}$$

where $R_n = kU_n + lV_n$ and $R_B = d_1R_1 + d_2R_2 + d_3R_3 \equiv kU_B + lV_B$. The eigenfunctions satisfy

$$\phi_1/\phi_2 = (R_1 - \sigma)/(R_2 - \sigma - d_1k),$$

$$\phi_3/\phi_2 = (R_3 - \sigma)/(R_2 - 2\sigma - d_3k). \tag{D.3}$$

Given a forcing of frequency ω, the group velocity and wave rays of three wave modes can be solved numerically as in section 3. It is found that one mode always propagates westward rapidly, resembling the N mode. The other two modes, however, tend to follow the ventilation flow, resembling the A mode.

The major features of the wave propagation can be seen analytically in the low-frequency limit $\omega \to 0$. As $\sigma = \omega \to 0$, the wavenumber solution can be derived from (D.1) and (D.2c) as $c_0 = 0$. One solution is obviously

$$k = 0, \qquad \text{N mode.} \tag{D.4}$$

With (D.4), the group velocity and wave structure can be derived as

$$C_{gN} = (\partial_k \sigma, \partial_l \sigma)_N = (-V_B/V_3, 0), \quad \text{N mode,} \quad \text{(D.5a)}$$

and

$$\phi_1/\phi_2 = V_1/V_2, \qquad \phi_3/\phi_2 = V_3/V_2, \quad \text{N mode.} \quad \text{(D.5b)}$$

Since the meridional flows are in the same direction in the interior wind driven thermocline, the wave propagates purely westward and has an equivalent barotropic structure. This is similar to the N mode of the 2.5-layer model discussed in section 3 [Eqs. (3.9a,b)].

The other two modes, which are advective modes, can be seen most clearly in the case of $d_1 = d_3$.[5] For convenience, (D.2c) is rewritten as

$$c_0 = k\{R_3(R_2 - d_1k)(R_B - d_2d_1k) - R_1(R_2 - d_3k)(R_B - d_2d_3k) - R_1R_3(d_3 - d_1) \times [R_2 + k(d_3 + d_1)]\}/(R_3 - R_1). \quad \text{(D.6)}$$

With $d_1 = d_3$, (D.6) immediately reduces to $c_0 = k(R_2 - d_1k)(R_B - d_2d_1k)$. The two advective modes are

$$R_2 - d_1k = 0, \quad \text{or}$$

$$(U_2 - d_1)k + V_2l = 0, \quad \text{A1 mode,} \quad \text{(D.7)}$$

and

$$R_B - d_2d_1k = 0, \quad \text{or}$$

$$(U_B - d_1d_2)k + V_Bl = 0, \quad \text{A2 mode.} \quad \text{(D.8)}$$

The group velocity for the two advective modes can be derived with the aid of (D.7) and (D.8), respectively, as

$$C_{gA1} = (\partial_k \sigma, \partial_l \sigma)_{A1} = (U_2 - d_1, V_2)F_{A1}, \quad \text{A1 mode,} \quad \text{(D.9)}$$

$$C_{gA2} = (\partial_k \sigma, \partial_l \sigma)_{A2} = (U_B - d_1d_2, V_B)F_{A2}, \quad \text{A2 mode,} \quad \text{(D.10)}$$

where the speed factors are

$$F_{A1} = \frac{(U_1 + U_3)V_2 - (V_1 + V_3)(U_2 - d_1)}{(2U_1 + U_3)V_2 - (2V_1 + V_3)(U_2 - d_1)} \quad \text{(D.11)}$$

$$F_{A2} = 1\Big/\left(1 - \frac{[U_2V_B - V_2(U_B - d_1d_2)][U_3V_B - V_3(U_B - d_1d_2)]}{[(U_2 - d_1)V_B - V_2(U_B - d_1d_2)]V_B}\right). \quad \text{(D.12)}$$

Thus, the direction and speed of each wave ray is determined completely by the mean thermocline structure, but independent of wavenumber. The A1 and A2 modes are always parallel to $(U_2 - d_1, V_2)$ and $(U_B - d_1d_2, V_B)$, respectively, and therefore are strongly influenced by mean flow advection, in sharp contrast to the N mode in (D.5a). The A1 mode is always more westward than layer-2 ventilation flow. The A2 mode is parallel to the wave characteristics as does the A mode in the 2.5-layer model [see section 3, Eq. (3.10a,b)]. If the mean flow is weak in layer 3 (e.g., shadow zone of layer 3), the wave characteristics are parallel to, but slower than, the mean ventilation flow of layer 2 as discussed in (6.2) is

$$(U_2, V_2) = (U_B - d_1d_2, V_B)(1 + d_1/d_2). \quad \text{(D.13)}$$

Now, the A2 mode wave ray is parallel to layer-2 ventilation flow, with the A1 mode wave ray somewhat westward. The speed factors F_{A1} and F_{A2} vary in different regions of the mean thermocline circulation. However, in the case of very weak layer-3 flow [shadow zone in layer 3, $(U_3, V_3) = 0$], (D.11) and (D.12) reduce to $F_{A1} = \frac{1}{2}$ and $F_{A2} = 1$, respectively. Therefore, the A1 mode is about half the speed of layer-2 flow. The A2 mode is the same speed as the wave characteristics, which, notice (D.13), is slower than layer-2 ventilation flow. Consistent with the A mode in the 2.5-layer model, both advective modes are slower than the middle thermocline ventilation flow.

It can be shown that the wave structure of the A2 mode has no barotropic transport $d_1\phi_1 + d_2\phi_2 + d_3\phi_3 = 0$, with ϕ_2 the opposite sign as the other two. This is reminiscent of the mode 3 structure. The wave structure of the A1 mode is more complex; it has virtually no currents in layer 2: $\phi_2/\phi_1 = \phi_2/\phi_3 \to 0$; and $\phi_3 \ll \phi_1$ if layer-3 flow is weak. Thus, the A1 mode is surface trapped, which has no apparent analogy of free wave structure. Finally, notice in (D.7), (D.9), (D.8), and (D.10) that the wave vector (k, l) is always normal to the wave ray. In other words, particles move parallel to the wave ray—a consequence of the limit of low-frequency planetary wave.

[5] The two other simpler cases are $U_3 = V_3\ (=R_3) = 0$ and $U_1 = V_1\ (=R_1) = 0$.

REFERENCES

Black, R., C. Rooth, D. Hu, and L. T. Smith, 1992: Salinity-driven thermocline transients in a wind- and thermohaline-forced iso-

pycnal coordinate mode of the North Atlantic. *J. Phys. Oceanogr.,* **22,** 1486–1505.
Chelton, D. B., and M. G. Schlax, 1996: Global observations of oceanic Rossby waves. *Science,* **272,** 234–238.
Deser, C., M. A. Alexander, and M. S. Timlin, 1996: Upper-ocean thermal variations in the North Pacific during 1970–1991. *J. Climate,* **9,** 1840–1855.
Dewar, W., 1989: A theory of time-dependent thermocline. *J. Mar. Res.,* **47,** 1–31.
——, 1998: On ''too–fast'' baroclinic planetary waves in the general circulation. *J. Phys. Oceanogr.,* **28**, 1739–1758.
Gu, D., and S. G. H. Philander, 1997: Interdecadal climate fluctuations that depend on exchanges between the tropics and extratropics. *Science,* **275,** 805–807.
Hendershott, M. C., 1989: The ventilated thermocline in quasigeostrophic approximation. *J. Mar. Res.,* **47,** 33–53.
Hoskins, B. J., and D. Karoly, 1981: The steady linear response of a spherical atmosphere to thermal and orographic forcing. *J. Atmos. Sci.,* **38,** 1179–1196.
Huang, R. X., and J. Pedlosky, 1998: Climate variability inferred from a layered model of the ventilated thermocline. *J. Phys. Oceanogr,* **29**, 779–790.
Jacobs, G. A., H. E. Hurlburt, J. C. Kindle, E. J. Metzger, J. L. Mitchell, W. J. Teague, and A. G. Wallcraft, 1994: Decade-scale trans-Pacific propagation and warming effects of an El Niño anomaly. *Nature,* **370,** 360–363.
Joyce, T. M., and P. Robbins, 1996: The long-term hydrographic record at Bermuda. *J. Climate,* **9,** 3121–3131.
Killworth, P. D., D. B. Chelton, and R. A. de Szoeke, 1997: The speed of observed and theoretical long extratropical planetary waves. *J. Phys. Oceanogr.,* **27,** 1946–1966.
Latif, M., and T. P. Barnett, 1994: Causes of decadal climate variability over the North Pacific and North America. *Science,* **266,** 634–637.
Lau, N.-C., and M. J. Nath, 1996: The role of the ''atmospheric bridge'' in linking tropical Pacific ENSO events to extratropical SST anomalies. *J. Climate,* **9,** 2036–2057.
Levitus, S., 1982: *Climatological Atlas of the World Ocean.* NOAA Professional Paper No. 13, 173 pp.
Lighthill, J., 1979: *Waves in Fluid.* Cambridge University Press, 504 pp.
Liu, Z., 1993a: Thermocline forced by varying wind. Part I: Spin-up and spin-down. *J. Phys. Oceanogr.,* **23,** 2505–2522.
——, 1993b: Thermocline forced by varying wind. Part II: Annual and decadal Ekman pumping. *J. Phys. Oceanogr.,* **23,** 2523–2541.
——, 1996: Thermocline variability in different dynamic regions. *J. Phys. Oceanogr.,* **26,** 1633–1645.
——, 1998: Planetary waves in thermocline circulation: Non-Doppler-shift mode, advective mode and Green mode. *Quart. J. Roy. Meteor. Soc.,* in press.
——, and J. Pedlosky, 1994: Thermocline forced by annual and decadal surface temperature variation. *J. Phys. Oceanogr.,* **24,** 587–608.
——, S. G. H. Philander, and R. Pacanowski, 1994: A GCM study of tropical–subtropical upper-ocean mass exchange. *J. Phys. Oceanogr.,* **24,** 2606–2623.
Luyten, J., and H. Stommel, 1986: Gyres driven by combined wind and buoyancy flux. *J. Phys. Oceanogr.,* **16,** 1551–1560.
——, J. Pedlosky, and H. Stommel, 1983: The ventilated thermocline. *J. Phys. Oceanogr.,* **13,** 292–309.
Marshall, D., and J. Marshall, 1995: On the thermodynamics of subduction. *J. Phys. Oceanogr.,* **25,** 138–151.
McCreary, J. P., and P. Lu, 1994: On the interaction between the subtropical and the equatorial oceans: The subtropical cell. *J. Phys. Oceanogr.,* **24,** 466–497.
Miller, A. J., D. R. Cayan, and W. B. White, 1998: A westward intensified decadal change in the North Pacific thermocline and gyre-scale circulation. *J. Climate,* **11,** 3112–3127.
Nurser, G., and J. Marshall, 1991: On the relationship between subduction rates and diabatic forcing of the mixed layer. *J. Phys. Oceanogr.,* **21,** 1793–1802.
Pedlosky, J., 1987: *Geophysical Fluid Dynamics.* 2d ed. Springer-Verlag, 710 pp.
Rhines, P. B., 1986: Vorticity dynamics of the oceanic general circulation. *Ann. Rev. Fluid Mech.,* **18,** 433–447.
——, and W. R. Young, 1982: A theory of the wind-driven circulation. Part I: Mid-ocean gyres. *J. Mar. Res.,* **40** (Suppl.), 559–596.
Schneider, N., A. J. Miller, M. A. Alexander, and C. Deser, 1998: Subduction of decadal North Pacific temperature anomalies: Observations and dynamics. *J. Phys. Oceanogr.,* **29**, 1056–1070.
Singh, A., 1997: Planetary wave instability in the thermocline circulation. M. S. thesis, Department of Atmospheric and Oceanic Sciences, University of Wisconsin-Madison, 44 pp.
Sturges, W., and B. G. Hong, 1995: Wind forcing of the Atlantic thermocline along 32oN at low frequencies. *J. Phys. Oceanogr.,* **25,** 1706–1714.
Wallace, J. M., and D. S. Gutzler, 1981: Teleconnections in the geopotential height field during the Northern Hemisphere winter. *Mon. Wea. Rev.,* **109,** 784–812.
White, B. W., and D. R. Cayan, 1997: Quasi-periodicity and global symmetries in interdecadal upper ocean temperature variability. *J. Geophys. Res.,* submitted.
Zhang, L. P., 1998: Study thermocline variability with an intermediate layered model. M.S. thesis, Department of Atmospheric and Oceanic Sciences, University of Wisconsin-Madison, 61 pp.
Zhang, R.-H., and S. Levitus, 1997: Structure and cycle of decadal variability of upper ocean temperature in the North Pacific. *J. Climate,* **10,** 710–727.
——, and Z. Liu, 1999: Decadal thermocline variability in the North Pacific Ocean: Two anomaly pathways around the subtropical gyre. *J. Climate,* in press.